Naval Research Laboratory

Barotropic Flow in the Vicinity of an Idealized Inlet — Simulations with the ADCIRC Model

JAYARAM VEERAMONY

Center for Oceanic and Atmospheric Modeling
University of Southern Mississippi
Stennis Space Center, MS 39529

CHERYL ANN BLAIN

Ocean Dynamics and Prediction Branch
Oceanography Division

March 9, 2001

20010402 058

Naval Research Laboratory

REPORT DOCUMENTATION PAGE

Public reporting burden for this collection of information is estimated to average 1 hour per response, including the time for reviewing instructions, searching existing data sources, gathering and maintaining the data needed, and completing and reviewing the collection of information. Send comments regarding this burden estimate or any other aspect of this collection of information, including suggestions for reducing this burden, to Washington Headquarters Services, Directorate for Information Operations and Reports, 1215 Jefferson Davis Highway, Suite 1204, Arlington, VA 22202-4302, and to the Office of Management and Budget, Paperwork Reduction Project (0704-0188), Washington, DC 20503.

1. AGENCY USE ONLY (Leave Blank)	2. REPORT DATE	3. REPORT TYPE AND DATES COVERED
	March 9, 2001	

4. TITLE AND SUBTITLE

Barotropic Flow in the Vicinity of an Idealized Inlet—Simulations with the ADCIRC Model

5. FUNDING NUMBERS

PE-0602435N

6. AUTHOR(S)

Jayaram Veeramony* and Cheryl Ann Blain

7. PERFORMING ORGANIZATION NAME(S) AND ADDRESS(ES)

Naval Research Laboratory
Stennis Space Center, MS 39529

8. PERFORMING ORGANIZATION REPORT NUMBER

NRL/FR/7320--01-9977

9. SPONSORING/MONITORING AGENCY NAME(S) AND ADDRESS(ES)

Naval Research Laboratory
4555 Overlook Ave., S.W.
Washington, DC 20375-5320

10. SPONSORING/MONITORING AGENCY REPORT NUMBER

11. SUPPLEMENTARY NOTES

*Center for Oceanic and Atmospheric Modeling, University of Mississippi, Stennis Space Center, MS 39529

12a. DISTRIBUTION/AVAILABILITY STATEMENT

Approved for public release; distribution is unlimited.

12b. DISTRIBUTION CODE

13. ABSTRACT (Maximum 200 words)

The flow in the vicinity of an idealized tidal inlet is studied using the nonlinear finite-element model ADCIRC. The principal aim is to establish a database of results to identify, analyze, and explain the processes in and near tidal inlets of the Mississippi Sound region in the northeast Gulf of Mexico. Coastal waters in the northeast Gulf of Mexico are forced by a combination of tides, river runoff, and wind. The effects of these forcings, and that of advection, Coriolis acceleration, and barrier islands are studied. The two-dimensional (2D) depth-averaged results derived from the three-dimensional (3D) model computations are similar to those computed by the 2D model for the tidally driven flow, whereas they are significantly different for the wind- and river-induced flow. Counter-rotating eddies are produced by tides when convective terms are included in the simulation. Coriolis acceleration accounts for the asymmetry within and outside the inlet. The flow in the region is weakly nonlinear. The wind- and river-induced flows contribute mainly to the residual circulation. Both the magnitude and the direction of the flow change from the surface to the bottom. The presence of the barrier island modifies the direction of the tidally induced flow in the inlet.

14. SUBJECT TERMS

Idealized and bays	ADCIRC	
River runoff	Wind	
Tides		

15. NUMBER OF PAGES

30

16. PRICE CODE

17. SECURITY CLASSIFICATION OF REPORT	18. SECURITY CLASSIFICATION OF THIS PAGE	19. SECURITY CLASSIFICATION OF ABSTRACT	20. LIMITATION OF ABSTRACT
UNCLASSIFIED	UNCLASSIFIED	UNCLASSIFIED	UL

CONTENTS

BAROTROPIC FLOW IN THE VICINITY OF AN IDEALIZED INLET — SIMULATIONS WITH THE ADCIRC MODEL

INTRODUCTION

The circulation and exchange processes in the vicinity of tidal inlets determine, to a large extent, the direction of sediment transport (David and Kjerfve 1998), the movement of larvae and plankton, and the fate of pollutants and other land-derived material (Signell and Butman 1992). Tidal inlets are usually short, shallow channels connecting a semi-enclosed body of water such as an estuary or a bay to the coastal ocean. The flow in these channels and in the nearby regions is forced predominantly by tides, even though other forcing mechanisms such as wind, waves, river runoff, and stratification can be important.

Idealized inlet geometries have been used by various investigators to study different aspects of the circulation near tidal inlets. Awaji et al. (1980) and Imasato et al. (1980) studied tidal exchange through a narrow strait, using a simple model basin forced with semidiurnal tides. The rapid spatial changes in tidal velocities were found to cause the exchange of an extremely large amount of water through the strait. The tidally induced residual circulation in the vicinity of the inlet also played an important part in the exchange process. They conclude that the major component of the exchange through narrow inlets is the result of the dynamical processes associated with tides. Awaji et al. (1982) found that small-scale turbulent fluctuations have a relatively small impact in the vicinity of tidal inlets and that tidally induced dispersion is dominant.

Kapolnai et al. (1996) studied the circulation in the vicinity of an idealized tidal inlet forced by an M_2 tide and a weakly buoyant river discharge. Significant differences in the residual current field were found to result from the presence of stratification. Wheless and Valle-Levinson (1996) also studied tidally driven estuarine exchange through a narrow inlet using a domain similar to Kapolnai et al. (1996). Again, semidiurnal tides and buoyancy differential supplied the forcing. They found the near-bottom transport to be directed toward the inlet mouth near the seaward side of the inlet. They also found that asymmetric tidally induced eddies on either side of the inlet contribute to the circulation.

The principal aim of this study is to establish a database of results for an idealized tidal inlet that can be used to identify, analyze, and explain the processes in and near tidal inlets of the Mississippi Sound region in the northeast Gulf of Mexico. Coastal waters in the northeast Gulf of Mexico are forced by a combination of tides, river outflow, and wind. The hydrodynamics in the vicinity of the idealized inlet are modeled using the nonlinear, finite-element model ADCIRC-2DDI/3D. One advantage of a finite-element model is that resolution throughout the domain can be varied. This allows increased resolution in the shallow regions while keeping coarser resolution in deeper waters, which leads to savings in computational time. The advantage of accurately modeling the coastal outline using the irregular grid structure is secondary in this study where only idealized domains are considered. Blain and Rogers (1998) conducted in-depth validation studies for the coastal tidal prediction using the 2D, depth-integrated

ADCIRC-2DDI model, which illustrated the influence of nonlinearities, forcing, and the sensitivity of model parameters. The model has also been applied to a number of field studies with excellent results (Westerink et al. 1992a, 1994; Kolar 1994a, b).

This report is organized into several main sections. We start with a very brief description of the model. The two- and three-dimensional equations are presented, along with a discussion of the principal features of the model, including the bottom friction parameterization, the representation of horizontal and vertical mixing, and the eddy viscosity model used. The solution procedure for the 3D model is also briefly stated. This is followed by a description of the computational domain, including the reasons for choosing input parameters associated with tidal elevations, wind stress, and river runoff. A preliminary analysis of the modeled dynamics focuses on the effect of the mesh resolution and forcing frequency. Computed residual currents forced by tides are used to compare the 2D vs 3D model solutions. In the next section, the role of individual terms in the momentum equation on circulation dynamics is investigated. A range of forcings is considered, as is the presence of a barrier island. Emphasis is placed on understanding 3D flow field as a response to the modeled dynamics. This is followed by a brief conclusion of the findings.

MODEL DESCRIPTION

The hydrodynamic computations in this study were performed using the ADvanced CIRCulation model (ADCIRC). This model is based on the three-dimensional Reynolds equations, simplified using the Boussinesq approximation as well as the hydrostatic pressure approximation. The model includes options for solving either the depth-integrated (ADCIRC-2DDI) or the three-dimensional (ADCIRC-3D) equations. The assumption of hydrostatic pressure implies, however, that the model is accurate for flows that are only weakly three-dimensional, i.e., the vertical variation of velocity is small in comparison to the horizontal variation. Important model features are summarized below. Further details can be obtained from Leuttich et al. (1992), Westerink et al. (1992b), and Kolar et al. (1994b).

The equations are written in a "σ" coordinate system, with the free surface at $\sigma = a$ and the bottom at $\sigma = b$, where a and b are constants for the domain. The number of points in the vertical remains the same throughout the domain regardless of the variation in water depth, which implies that the vertical resolution is a function of the water depth. Thus, the equations used in the ADCIRC-3D model are

$$\frac{\partial \zeta}{\partial t} + \frac{\partial (uH)}{\partial x} + \frac{\partial (vH)}{\partial y} + \frac{\partial (wH)}{\partial \sigma} = 0, \tag{1}$$

$$\frac{\partial u}{\partial t} + u\frac{\partial u}{\partial x} + v\frac{\partial u}{\partial y} + w\frac{\partial u}{\partial \sigma} - fv = -\frac{\partial}{\partial x}\left[\frac{p_s}{\rho_0} + g(\zeta - \alpha\eta)\right] + \frac{(a-b)}{H}\frac{\partial}{\partial \sigma}\left(\frac{\tau_{zx}}{\rho_0}\right) + m_x, \tag{2}$$

$$\frac{\partial v}{\partial t} + u\frac{\partial v}{\partial x} + v\frac{\partial v}{\partial y} + w\frac{\partial v}{\partial \sigma} + fu = -\frac{\partial}{\partial y}\left[\frac{p_s}{\rho_0} + g(\zeta - \alpha\eta)\right] + \frac{(a-b)}{H}\frac{\partial}{\partial \sigma}\left(\frac{\tau_{zy}}{\rho_0}\right) + m_y, \tag{3}$$

$$\frac{\partial p}{\partial \sigma} = -\frac{\rho g H}{(a-b)}, \tag{4}$$

where t represents time; x, y are the horizontal Cartesian coordinate directions; ζ is the free surface elevation relative to the geoid; u and v are the horizontal velocities; w is the vertical velocity; h is the bathymetric depth relative to the geoid; $H = \zeta + h$ is the total water column depth; f is the Coriolis parameter; p_s is the atmospheric pressure at the free surface; g is the acceleration due to gravity; α is the effective Earth elasticity factor; η is the Newtonian equilibrium tide potential; ρ_0 is the reference density

of water; m_x and m_y are the horizontal momentum diffusion/dispersion terms; and τ_{zx} and τ_{zy} are the vertical shear stresses.

The shear stresses are parameterized in terms of the velocity field using eddy viscosity relationships of the form:

$$\tau_{zx} = \rho_0 E_v \frac{\partial u}{\partial z}, \tag{5}$$

$$\tau_{zy} = \rho_0 E_v \frac{\partial v}{\partial z}, \tag{6}$$

where E_v is the eddy viscosity.

Integrating the three-dimensional equations over the vertical (i.e., $\sigma = a$ to $\sigma = b$) yields the 2D depth-integrated version of the model. The three equations for unknowns, U, V, and ζ, in non-conservative form are

$$\frac{\partial \zeta}{\partial t} + \frac{\partial (UH)}{\partial x} + \frac{\partial (VH)}{\partial y} = 0, \tag{7}$$

$$\frac{\partial U}{\partial t} + U \frac{\partial U}{\partial x} + V \frac{\partial U}{\partial y} - fV = -\frac{\partial}{\partial x}\left[\frac{p_s}{\rho_0} + g(\zeta - \alpha \eta)\right] + \frac{M_x}{H} + \frac{D_x}{H} + \frac{\tau_{sx}}{\rho_0 H} - \frac{\tau_{bx}}{\rho_0 H}, \tag{8}$$

$$\frac{\partial V}{\partial t} + U \frac{\partial V}{\partial x} + V \frac{\partial V}{\partial y} + fU = -\frac{\partial}{\partial x}\left[\frac{p_s}{\rho_0} + g(\zeta - \alpha \eta)\right] + \frac{M_y}{H} + \frac{D_y}{H} + \frac{\tau_{sy}}{\rho_0 H} - \frac{\tau_{by}}{\rho_0 H}, \tag{9}$$

where U and V are the depth-averaged velocity; M_x and M_y are the depth-integrated horizontal momentum diffusion terms; D_x and D_y are the depth-integrated horizontal momentum dispersion terms; τ_{sx} and τ_{sy} are the applied horizontal free surface stresses; and τ_{bx} and τ_{by} are the horizontal bottom stress terms. The continuity equation (5) is reformulated into a generalized wave continuity equation (GWCE) (Lynch and Gray 1979; Kinnmark 1984). The equations are then discretized using the finite-element method (Kolar et al. 1994a).

Bottom stress terms are parameterized using the standard quadratic friction law:

$$\tau_{bx} = C_f \rho_0 \left(U^2 + V^2\right)^{1/2} U, \tag{10}$$

$$\tau_{by} = C_f \rho_0 \left(U^2 + V^2\right)^{1/2} V, \tag{11}$$

where C_f is the bottom friction coefficient. Lateral mixing due to diffusion and dispersion is represented through the simplified eddy viscosity formulation (Kolar and Gray 1990):

$$M_x + D_x = E_h^{MD}\left[2\frac{\partial^2 UH}{\partial x^2} + \frac{\partial^2 UH}{\partial y^2}\right], \tag{12}$$

$$M_y + D_y = E_h^{MD}\left[2\frac{\partial^2 VH}{\partial x^2} + \frac{\partial^2 VH}{\partial y^2}\right], \tag{13}$$

where E_h^{MD} is the horizontal eddy viscosity coefficient for momentum diffusion/dispersion. The wetting and drying of computational elements for predicting the movement of the shoreline is possible in ADCIRC, but this option is not exercised in these studies.

To minimize the computational effort in solving the three-dimensional equations, a mode-splitting technique is used in which the depth-integrated "external mode" equations are solved for the free-surface displacement and the depth-averaged velocity. The "internal mode" equations, which account for the vertical transport of momentum, are forced by these solutions. The solutions to the internal mode equations yield the vertical profiles of the velocity. These velocity profiles are then used in the computations of the shear stresses (Eqs. (5) and (6)). Only one eddy viscosity formulation is considered here (Grenier et al. 1995):

$$E_v = \kappa u_* z_0, \qquad\qquad z = -h, \tag{14}$$

$$E_v = \kappa u_* (z_0 + H), \qquad z > -h, \tag{15}$$

where $z = -h$ is the bottom; $\kappa = 0.41$ is the von Karman constant; u_* is the shear velocity; H is the distance from the bottom; and z_0 is the bottom roughness. Thus, the parameterizations of the bottom stress and the horizontal dispersion used in the two-dimensional model are no longer necessary. The horizontal momentum diffusion terms are retained to provide numerical stability and are parameterized with an expression identical to that of the two-dimensional model. The internal mode equations do, however, require the parameterization of the vertical turbulent momentum transport. The vertical momentum transport is calculated using an eddy viscosity formulation. Only one such formulation is considered here.

COMPUTATIONAL DOMAIN AND INPUT PARAMETERS

The idealized embayment setting given by Kapolnai et al. (1996) is representative of the geometry of the tidal inlets and bays in the Mississippi Sound and, hence, was adopted for the present study. Figure 1(a) shows the plan view of the computational domain. The smaller basin in the figure represents the sound, and the larger basin is the coastal ocean situated on the continental shelf. An inlet 2000 m wide and 3000 m long connects the two basins. The depth in the coastal ocean increases from 5 m at the mouth of the inlet to 14 m at the offshore boundary. The depth in the inlet and in the sound is constant at 5 m.

Figure 1(b) shows the identical plan view of the domain, but now with a barrier island offshore of the inlet. The 6000-m long barrier island has a width of 1000 m and is located 1250 m away from the mouth of the inlet, centered along the centerline of the inlet. All other dimensions of the domain are the same as for the case without the barrier island. In the discussions to follow, the positive y-direction implies northward orientation.

Tidal forcing is applied for these small domain simulations through a modulation of the boundary elevations. Tide enters the domain through the offshore boundary. At each boundary node, the amplitude and phase (i.e., the direction of propagation of the tide as it enters the domain) of the tidal constituent are assigned. For simulations that include tidal forcing, an M_2 tide with amplitude of 0.15 m, incident normal to the boundary (zero phase) is specified. The choice of the tidal amplitude is based on the amplitudes observed offshore near Biloxi, Mississippi (U.S. Army Corps of Engineers water level data). Although the tides in the Gulf of Mexico are primarily diurnal, for these simulations a semidiurnal tidal frequency is used. It is shown later that the flow characteristics are essentially the same regardless of the tidal frequency.
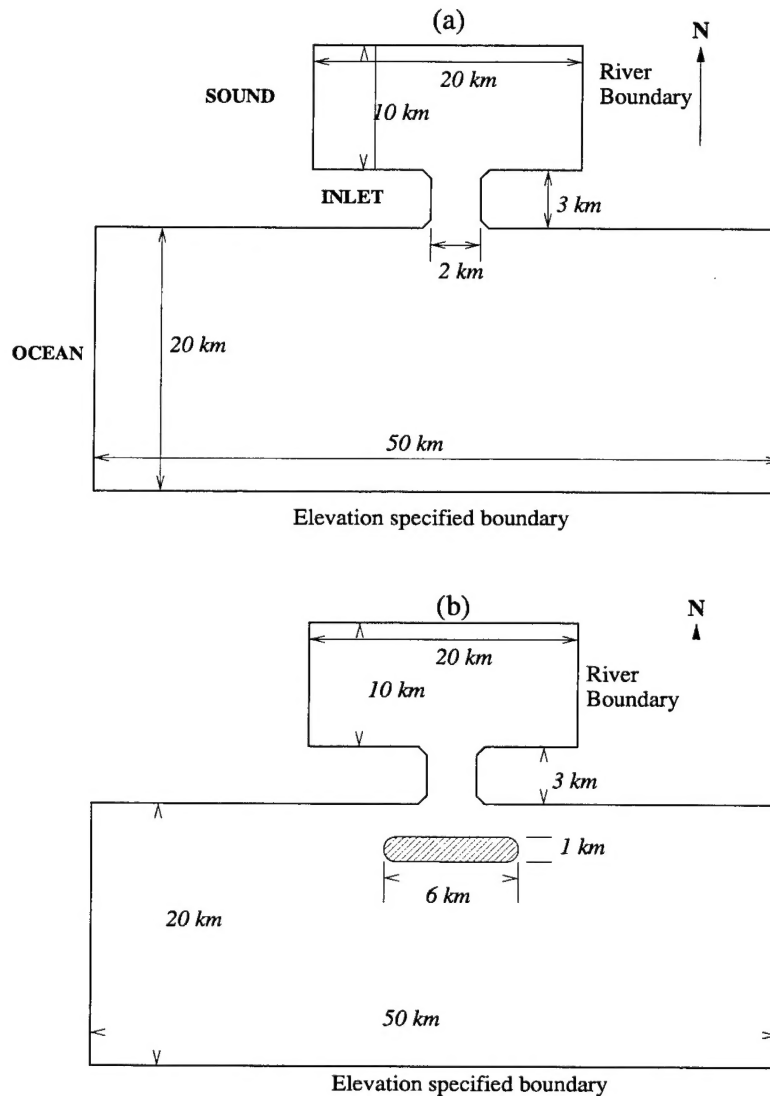
Fig. 1 – Plan view of the domain: (a) Without barrier island; (b) With barrier island

In addition to the tidal forcing, the effect of wind can be included in the model by specifying a surface shear stress. In simulations that include wind, a surface wind stress that induces a steady surface velocity of about 0.05 m/s in the inlet region is applied. The magnitude of the wind stress specified is representative of that observed in the Gulf of Mexico under "no storm" conditions. Wind stress is specified at grid nodes over the entire domain, including the region of the sound.

For simulations involving river outflow, the river mouth is specified at the eastern boundary of the sound. The river discharge rate of 50 m³/s is distributed evenly along the entire boundary and is of the same order of magnitude as the average outflow from the Wolf River into the Bay St. Louis, Mississippi, over the last 30 years (approximately 60 m³/s; USGS stream flow data). The remaining boundaries that do not have incoming flow specified are treated as wall boundaries.

In the following computations, it is assumed that the latitude of the center of the domain corresponds to that of the northern Gulf of Mexico (30°N). The Coriolis parameter f (= $2\Omega \sin\theta$, where Ω is the angular frequency of the Earth's rotation and θ is the latitude) corresponding to this latitude is 0.00073/s. The Coriolis parameter is considered constant over the entire domain since variation of θ over the entire domain is small.

Aside from the physical forcing and the boundary conditions, the two-dimensional, depth-integrated ADCIRC model contains only two parameters that require specification, the coefficient of bottom friction and the coefficient of horizontal eddy viscosity. In the two-dimensional simulations, bottom friction can be parameterized using a linear or nonlinear relationship. We choose the nonlinear parameterization, with a constant coefficient C_f = 0.0025 over the entire domain. The horizontal eddy viscosity coefficient has a constant value of E_h = 1.0 m²/s throughout the domain. This value of E_h is sufficient to deter the formation of instabilities, yet it is not large enough to significantly alter the magnitudes of the computed flow field throughout the domain.

In the simulations involving the three-dimensional model, the internal mode equations are solved using 11 horizontal levels. A bottom roughness coefficient of z_0 = 0.0005 is used in the computations. The roughness at the free surface is incorporated into the wind stress coefficient.

PRELIMINARY ANALYSIS

Effect of Mesh Resolution

Mesh resolution is an important aspect of any numerical study. Most models give increasingly accurate results when the domain is refined. However, increasing the mesh resolution often increases computational time. The optimum resolution for the mesh is that which, in the minimum necessary computational time, gives results whose accuracy cannot be significantly improved with further refinement. A check for solution convergence with respect to grid resolutions is performed using these meshes:

1. Grid 1: 500-m resolution in the vicinity of the inlet and 1000-m resolution elsewhere in the domain (coarse resolution, Fig. 2(a)).

2. Grid 2: A maximum resolution of 100 m in the inlet, increased gradually to 1000-m resolution (fine resolution, Fig. 2(b)).

3. Grid 3: A maximum resolution of 50 m in the inlet, increased gradually to 500-m (double the resolution shown in Fig. 2(b)).

Note that the geometrically sharp corners at the mouths of the inlet are removed for all the grids.

The results are obtained using the depth-integrated model, ADCIRC-2DDI, as described previously. Coriolis acceleration term is ignored for this test. Forcing comes only from an M_2 tide with 0.15 m amplitude, propagating normal to the boundary. The computed solutions from all mesh resolutions are interpolated onto a uniform grid with 250-m resolution so that error measures between solutions can be easily calculated.

Figure 3(a) compares the residual circulations computed over the coarse and fine grids. Outside the inlet, both grids produce counter-rotating eddies at the entrances to the inlet, with the residual flow directed away from and along the center of the inlet. The magnitude of the velocity predicted by the coarse grid is slightly larger, especially closer to the walls. However, overall, the flows predicted are similar to each other. On the other hand, inside the inlet the coarse grid predicts velocity close to 180°
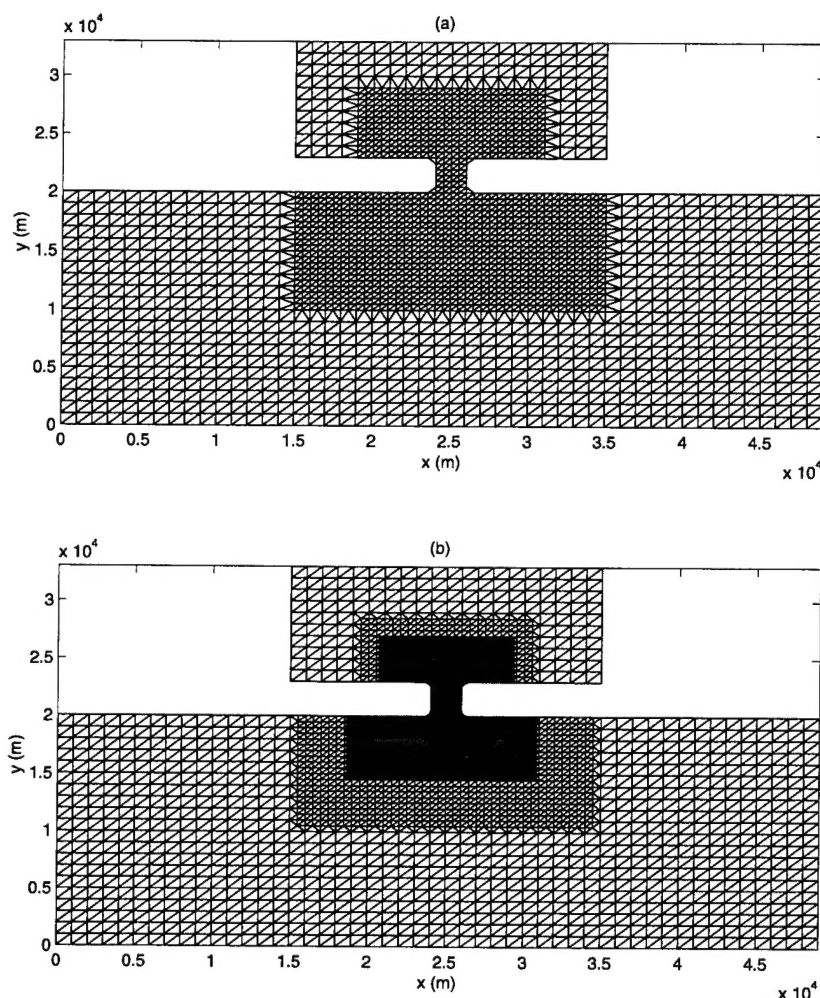
Fig. 2 – View of the grid resolutions: (a) "Coarse" grid with 500-m maximum resolution; (b) "Fine" grid with 100-m maximum resolution

out-of-phase at adjacent nodes, which leads to physically unrealistic velocity gradients. This "abnormality" disappears in computations over the fine grid. Amplitudes of the simulated M_2 tide are practically identical throughout the domain, regardless of mesh resolution. Figure 3(b) shows the difference between the predicted amplitudes. Figures 3(c) and (d) compare the modeled currents and elevations results using grid 2 with that computed over the grid with twice the resolution of the fine grid. The magnitude and direction of the residual currents (Fig. 3(c)) is nearly identical in both cases. Essentially, zero difference is observed in the magnitude of the M_2 tide (Fig. 3(d)) between grids.

The comparisons in Figs. 3(c) and (d) indicate that the fine grid yields a converged solution. Clearly, grid 1, which is a rather coarsely refined mesh, does not yield "realistic" flow characteristics in the vicinity of the inlet, although it may be sufficient for studying the tidal amplitudes and the flow farther away from the inlet. The differences in both the computed residual currents and tidal amplitudes between the fine grid (grid 2) and the very fine grid (grid 3) are extremely small. Thus, for this idealized system, we conclude that a 100-m resolution is necessary and sufficient to accurately model the flow, both inside and in the vicinity of the inlet. The fine grid mesh is used in all model experiments described hereafter.
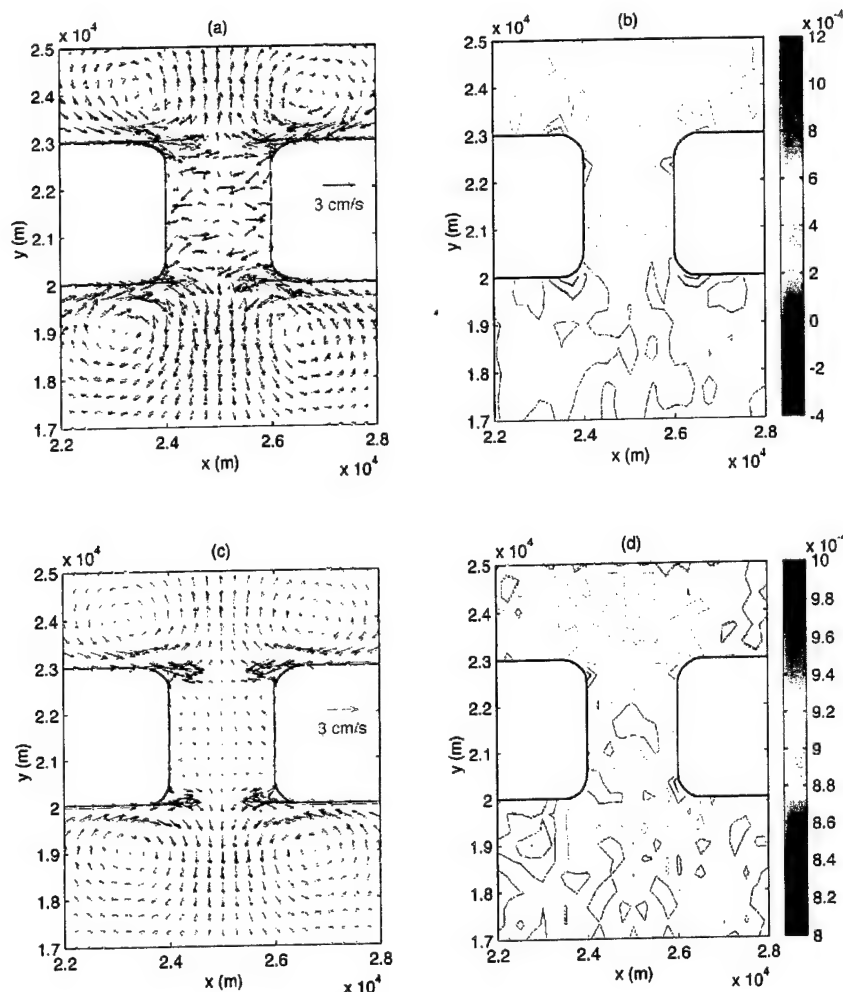
Fig. 3 – Comparison between "coarse" (blue) and "fine" (red) grid solutions: (a) Residual currents; (b) Difference in M_2 tidal amplitudes. Comparison between "fine" (blue) and "very fine" (red) grid solutions (c) Residual currents; (d) Difference in M_2 tidal amplitudes

Effect of Tidal Forcing Frequency

As mentioned in the introduction, this study aims to build a database of results for inlet circulation subject to various forcings, nonlinearities, and parameter values that can then be used to interpret field circulation patterns computed in the Mississippi Sound region. Diurnal tides (e.g., O_1) are dominant over semidiurnal tides (e.g., M_2) in the Gulf of Mexico. However, the advantage of using semidiurnal tides is that the model computations can be compared directly with those reported by other researchers who have studied the flow around idealized inlets (Awaji et al. 1980; Kapolnai et al. 1996). An additional advantage is that the computational time required to harmonically resolve the semidiurnal tides is about half of that necessary to resolve the diurnal tides. Here we show that the physical processes involved in the flow regime remain unchanged, regardless of the frequency of the incoming tide.

To demonstrate this, Fig. 4 compares the residual flow and the tidal amplitudes at the forcing frequency. Again, the depth-integrated model ADCIRC-2DDI is used to compute these results. Figures 4(a) and (b) how the residual currents and the tidal amplitude respectively, forced by an M_2 tide, and
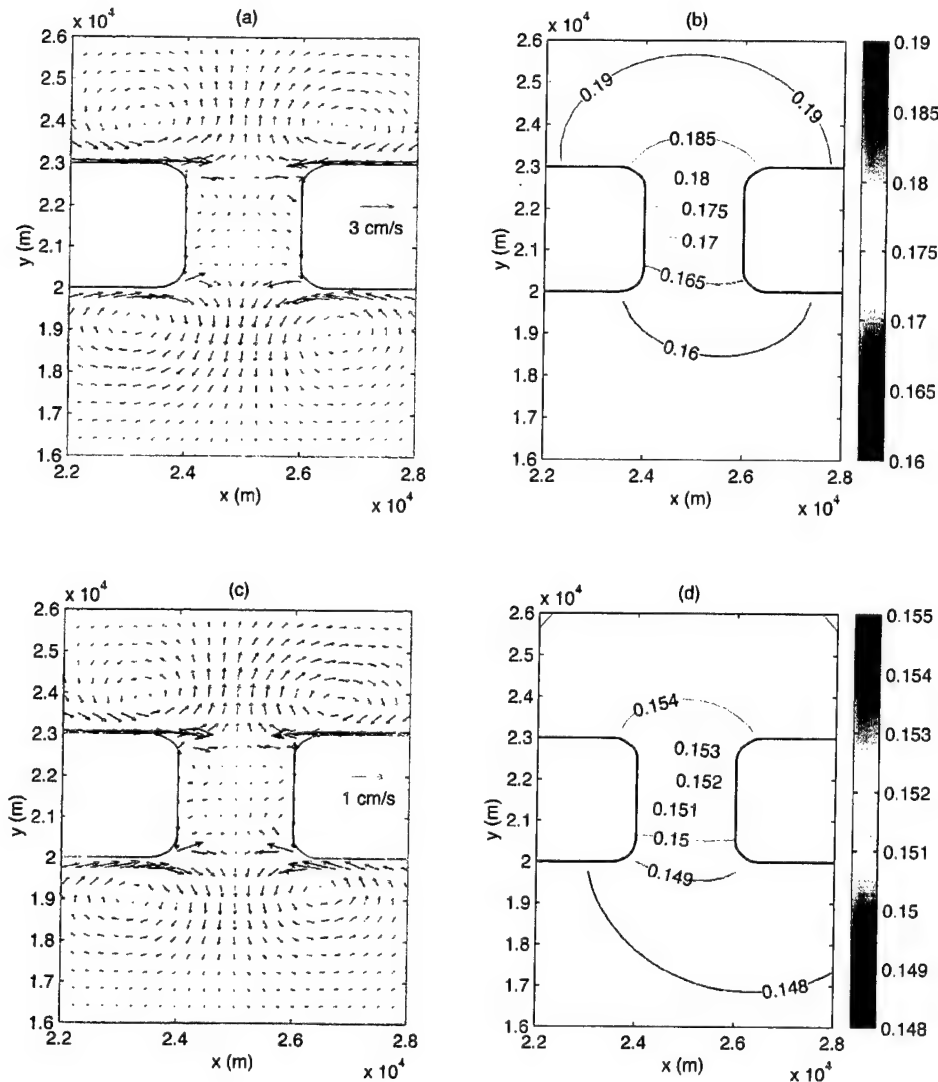
Fig. 4 – (a) Residual currents forced by an M_2 tide; (b) Amplitude contours of the M_2 tide;
(c) Residual currents forced by an O_1 tide; (d) Amplitude contours of the O_1 tide

Figs. 4(c) and (d) show that forced by an O_1 tide. The amplitude of both the M_2 and the O_1 tide at the offshore boundary is 0.15 m. In both cases, incoming tide is incident normal to the boundary.

The magnitude of the residual current due to the M_2 tide is larger in comparison to that forced by an O_1 tide, as is the increase in tidal amplitude in the inlet. The reason for this difference is that the frequency of the M_2 tide is larger than that of the O_1 tide. Therefore, the change in water depth over a tidal wavelength is smaller for the M_2 tide. The tidal elevation has more time to adjust to the shallowing water depth, which results in a larger increase in the tidal amplitude. This also implies a larger nonlinear effect. Thus, the shorter wavelength associated with the higher frequency wave, in turn, can produce larger magnitudes of the residual current. Despite this physical difference in the tidal waves, the residual currents produced by each frequency exhibit the same flow features. In particular, the counter-rotating eddies on either side of the inlet, both in the bay and on the continental shelf, are present. Also in both cases, amplitude contours inside the bay are symmetric about the centerline of the inlet. On the shelf-side, the asymmetry (which is explained later in this section) with respect to the centerline of the inlet is also reproduced in both cases, although the asymmetry is slightly more pronounced for the lower forcing

frequency. Thus, for all practical purposes, using the M_2 frequency as the input tidal forcing results in residual circulation and elevation patterns similar to those generated by an O_1 tidal frequency.

3D Model vs 2DDI Model

Extensive validation and sensitivity analysis of the two-dimensional, depth-integrated model (ADCIRC-2DDI) has been performed by a number of investigators. Blain and Rogers (1998) showed that the model gives excellent agreement when the observed velocities are compared to data at locations where the actual velocity is independent of depth. The difference in frictional characteristics between the 2D and the 3D models was reported by Grenier et al. (1995).

Here we compare the depth-averaged flow field computed by both ADCIRC-3D and the two-dimensional model, ADCIRC-2DDI. Figures 5(a) and 5(b) show the residual flow field and amplitude contours forced by an M_2 tide, computed by ADCIRC-2DDI and ADCIRC-3D respectively. Note that the 3D model computes a larger residual circulation and tidal amplification than that simulated by the 2DDI version of ADCIRC. This implies that the vertical velocity distribution affects, however slightly, the tidal amplitudes. The difference between the two models is more dramatically illustrated in Fig. 5(c), which shows the residual currents forced by an easterly wind. For the 2DDI model, the wind stress effectively acts over the entire water column. As a result, the current driven by the wind is directed eastward. Near the mouth of the inlet, some intrusion of the water from the coastal ocean is seen. In contrast, for the 3D model, wind stress is applied only at the surface, allowing the expected Ekman spiral to develop. Thus, the depth-averaged velocity is oriented to the right of the wind direction. This effect is discussed more in the next section. Figure 5(d) shows the river-induced flow in the domain. The direction of the flow on the shelf-side of the inlet is oriented more to the west in the solution computed by ADCIRC-2DDI. The effect of the Coriolis acceleration in the Northern Hemisphere is to cause the flow to turn right so as to preserve geostrophy. In comparison to the flow field computed by the 3D model, it is clear that the effect of Coriolis acceleration is enhanced in the 2DDI model.

Thus, ADCIRC-3D is able to reproduce the vertical structure of the residual current that is essential to the overall circulation dynamics in the vicinity of the inlet. Clearly, the 2D depth-integrated model is limited in its ability to accurately simulate currents in and around bays and inlets. ADCIRC-3D is used for all simulations presented hereafter.

RESULTS

Effect of Different Terms in the Momentum Equation

In ADCIRC-3D, the governing equations are written in a modular fashion. This allows the flexibility of turning off/on different terms in the momentum equations including various nonlinearities and model forcings. Here we study the effect of different physical forcing such as wind, tide, and river runoff, and additionally the sensitivity of the inlet system to the inclusion or exclusion of advection and Coriolis acceleration. The system is forced by an M_2 tide normally incident to the domain with 0.15-m amplitude at the offshore boundary.

Figure 6(a) shows the depth-averaged residual circulation and amplitude contours of the M_2 tide for a simulation that includes both Coriolis and convective acceleration terms. Outside the inlet, counter-rotating pairs of eddies are formed on the north and south side. Furthermore, the flow along the centerline of the inlet is directed away from the inlet. Inside the inlet, the flow is directed toward the center. A closer inspection of the residual currents show that the eddy on the southeastern side of the inlet has its center farther from the wall and more toward the middle of the inlet than the eddy at the southwestern side. The
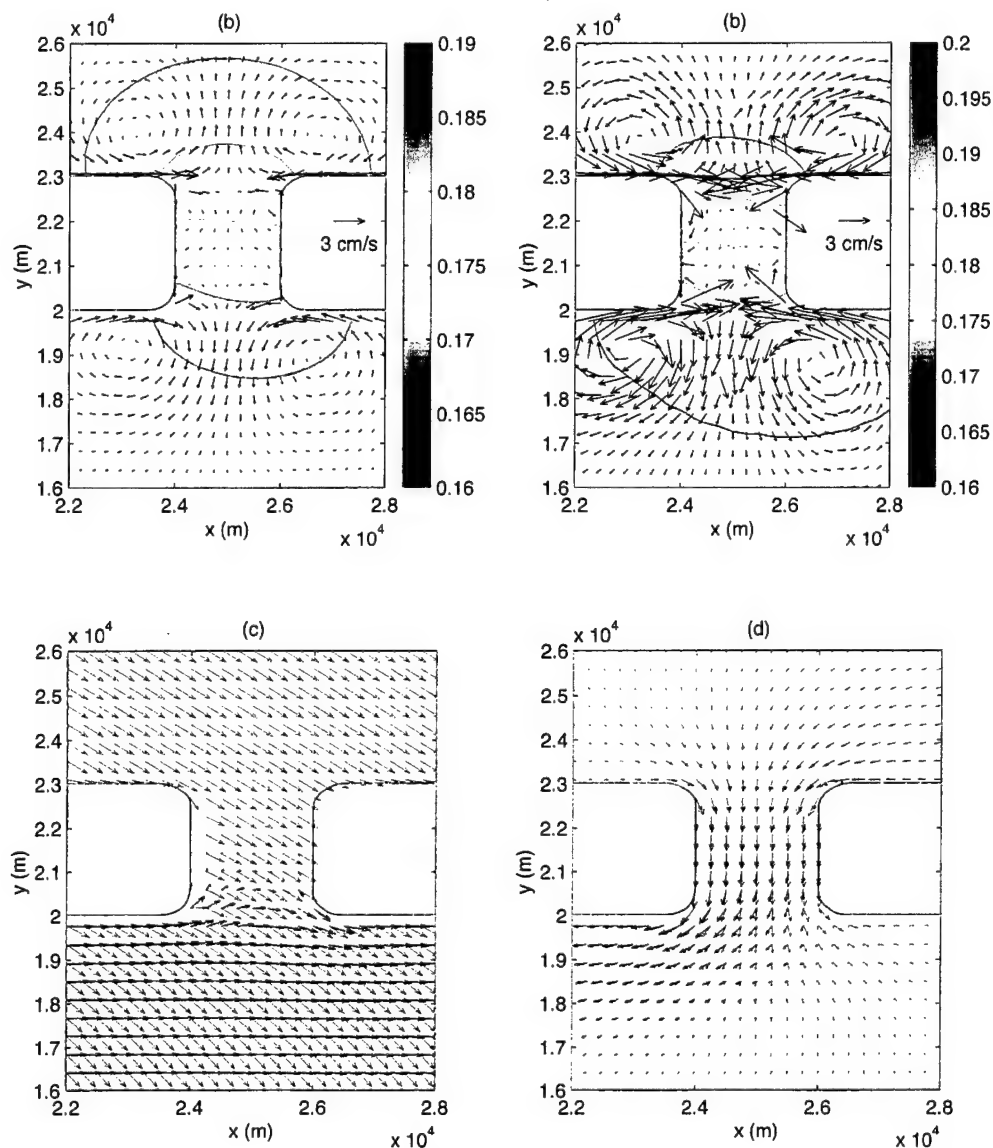
Fig. 5 – Comparison of tidally forced residual currents (black arrows) and amplitude contours:
(a) ADCIRC-2DDI; (b) ADCIRC-3D. Residual currents computed using ADCIRC-2DDI (blue) and
ADCIRC-3D (red): (c) Forced by wind; (d) Forced by river flow

M_2 amplitude increases from the open boundary toward the bay. The tidal amplification is extremely small on the south side of the inlet, in contrast to that inside the inlet, even though the depth is constant through the inlet. Again, the elevation contours are asymmetric about the centerline of the inlet in the south. In contrast, the counter-rotating eddies formed north of the inlet as well as the M_2 amplitude contours are symmetric about the centerline of the inlet.

Figure 6(b) shows the depth-averaged residual currents and the M_2 amplitudes for simulations in which the Coriolis acceleration alone is neglected. In contrast to the results in Fig. 6(a), the amplitude contours are symmetric about the centerline of the inlet throughout the domain. The residual velocity also shows perfect symmetry about the centerline of the inlet. The absence of the Coriolis acceleration terms is clearly indicated by this symmetry.
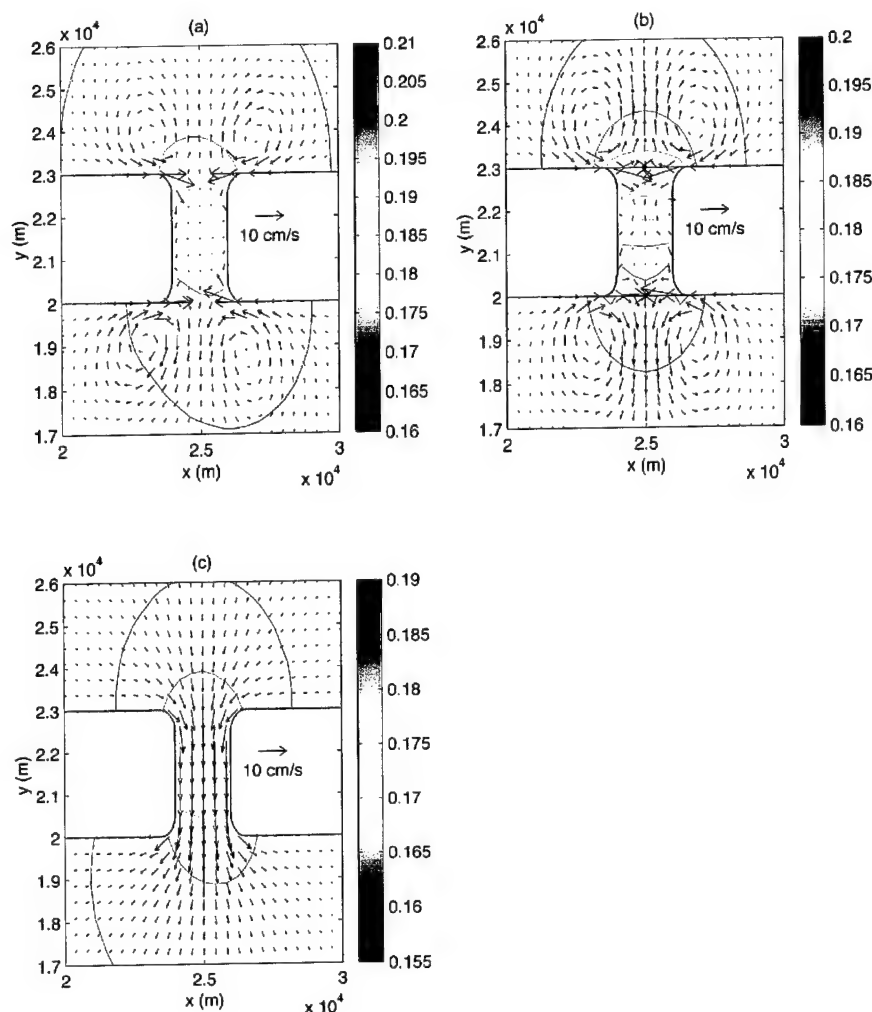
Fig. 6 – Residual flow field and M_2 amplitude contours (a) Including both Coriolis and convective
acceleration terms; (b) Only Coriolis term neglected; (c) Only convective acceleration neglected

Omitting the convective acceleration alone results in the residual flow field shown in Fig. 6(c). It is evident that the velocity vectors are significantly different from the two cases described above. Note, however, that the magnitudes of the tidal amplitude and residual currents are similar. First, we see that the counter-rotating eddies at the mouth of the inlet have completely disappeared, and the direction of the residual current in the entire domain is now oriented primarily toward the shelf. The magnitude of the residual current on the southwest side of the inlet is slightly larger than those observed on the southeast side. In contrast to the previous case, the amplitude contours south of the inlet are also asymmetric. The pressure gradient, which drives the flow, must therefore be larger on the west side of the inlet, resulting in an amplitude gradient that is also larger on the west side of the inlet.

Convective acceleration is responsible for the presence of counter-rotating eddies, even for the weakly nonlinear flows studied here. Coriolis terms account for asymmetry in elevation within and outside the inlet and are an important process even over such small areas.

Effect of Tides, Wind, and River Discharge

Now we consider the influence of various forcing mechanisms individually and in concert. First examined is the influence of tidal nonlinearity. Recall that Fig. 4(b) has the M_2 tidal amplitudes. Figure 7 shows the amplitudes of the M_4 (Fig. 7(a)) and M_6 (Fig. 7(b)) overtides for a simulation in which flow in the domain is forced by an M_2 tide. The M_4 overtide is produced by the nonlinear interaction of the M_2 tide with itself through the convective acceleration and nonlinear bottom friction terms. The M_6 overtide is a result of the interaction between the M_2 tide and the M_4 overtide. Amplitudes of the overtides are very small compared to those at the forcing frequency. The velocity field (not shown) is similarly small. Thus, the scenarios presented here fall into the regime of weakly nonlinear flows. The weak nonlinearity implies that the influence of wind and river discharge on the tidal amplitudes is minimal. This does not, however, imply that the nonlinear effects can be neglected completely. As was illustrated in Fig. 6, the absence of the convective acceleration terms in the momentum equations lead to the complete disappearance of the counter-rotating eddies.
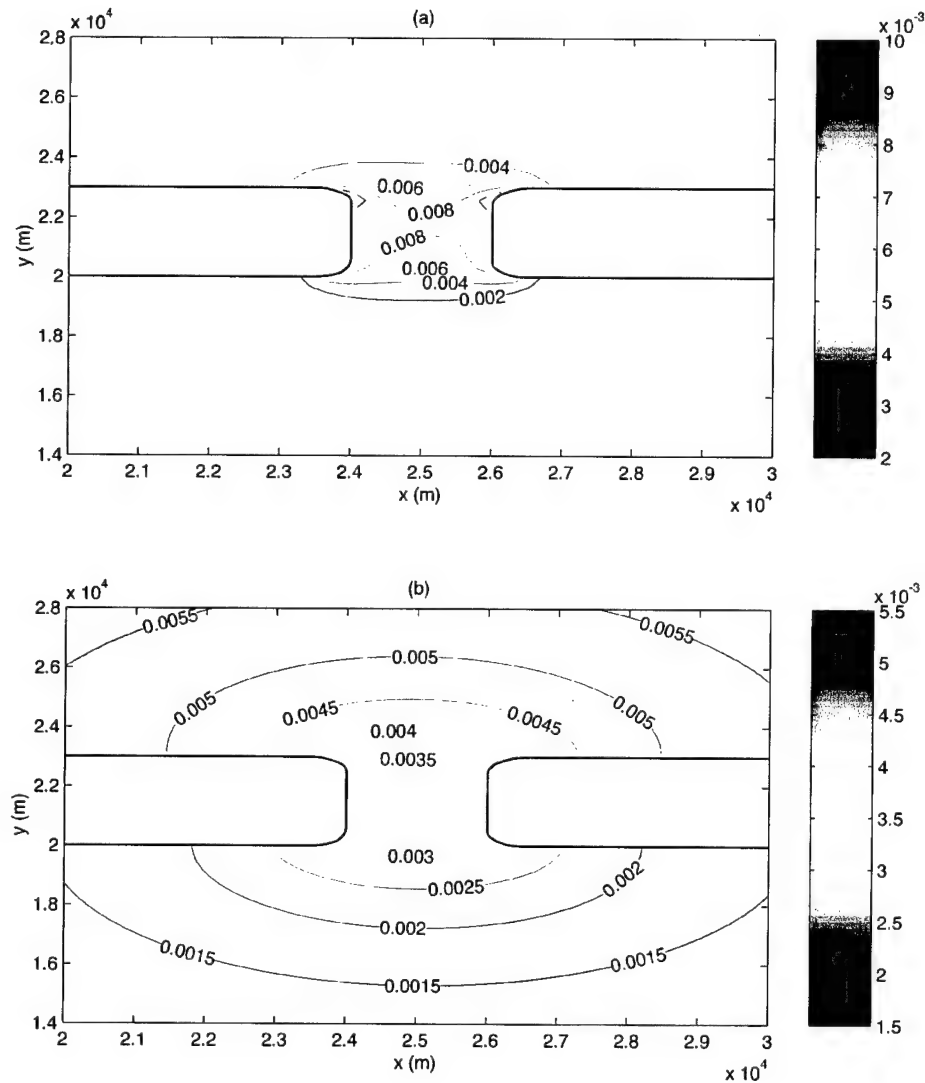

Fig. 7 – Amplitude contours of computed overtides forced by an M_2 tide: (a) M_4; (b) M_6

For the same M_2 forced solution, Fig. 8(a) shows the depth-averaged residual (also Fig. 6(a)). The counter-rotating eddies on the north side of the inlet are symmetric about the centerline of the inlet, with the current direction pointing northward at the center of the inlet. South of the inlet, however, the western gyre is slightly closer to the shoreline and farther away from the centerline than the eastern gyre. We also see that the flow south of the inlet along the centerline turns to the right due to the Coriolis effect previously discussed. The residual current in Fig. 8(b) is forced by the river discharge into the embayment, in the absence of either the wind or tide. The river runoff comes into the domain through the northeastern boundary (Fig. 1). North of the inlet, the flow converges toward the inlet. Due to the horizontal mixing, we see some flow entering the inlet from the northwest, but the predominant flow into the inlet is from the northeast. Flow exiting the inlet fans out with a small orientation to the west. Figure 8(c) shows the current residuals due to wind forcing only. The wind stress is applied uniformly over the entire domain. The magnitude of the depth-averaged velocity is of the same order as the velocity due to river inflow. North of the inlet and in the vicinity of the inlet on the south side, the wind-induced velocity is oriented 45° to the right of the wind direction. Close to the boundary, flow is directed offshore. This circulation pattern results because of mass conservation constraints. For an infinite ocean in the presence of wind, an Ekman spiral develops over the water column. The flow here is constrained by walls imposed along the eastern and western boundaries, forcing the flow out of the domain.
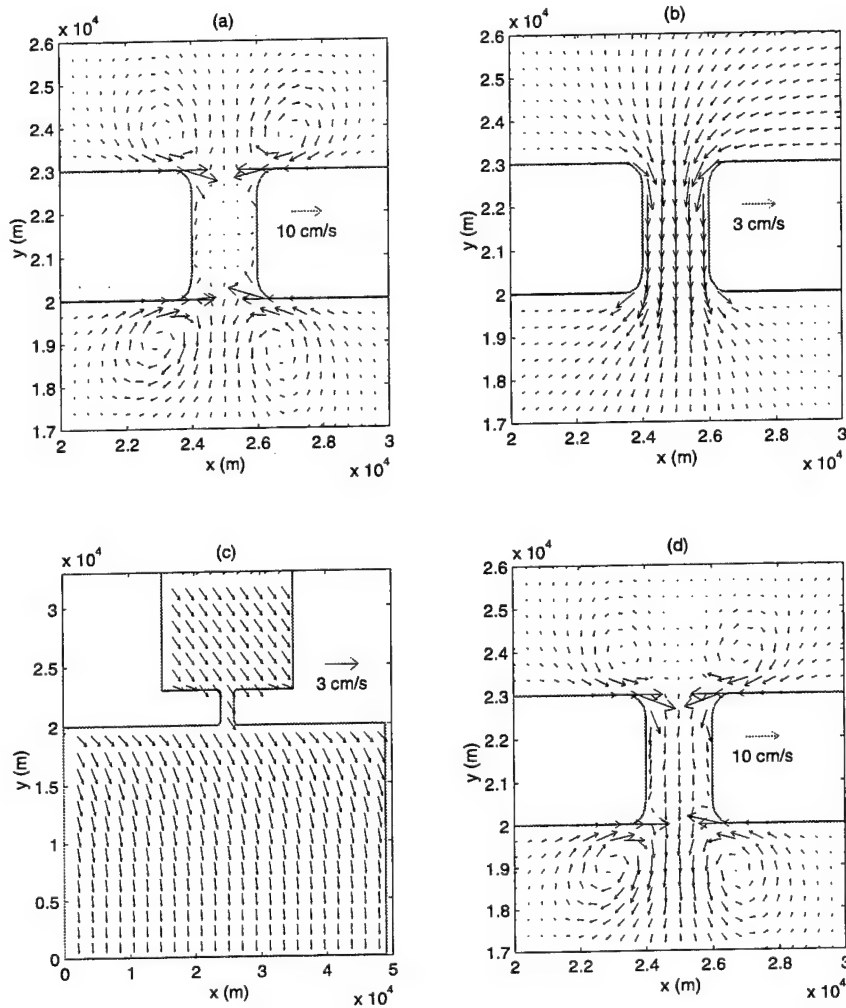

Fig. 8 – Residual velocities forced by (a) tide only; (b) river runoff only; (c) wind only;
(d) combination of tide, river runoff, and wind.

Finally, the residual circulation shown in Fig. 8(d) is due to the combined effect of the wind, river, and tidal forcing. First, we see that the magnitude of the current centered on the north side of the inlet is practically zero; current residuals due to the tidal, river, and wind forcing are in balance. The direction of the flow inside the inlet is toward the ocean. This was also noted by Kapolnai (1996), despite their application of a baroclinic model that excludes the effect of wind. South of the inlet, the flow direction is almost symmetric about the centerline of the inlet. The effect of Coriolis acceleration on the tide- and river-induced residuals is counterbalanced by its alteration of the wind-driven flow. As mentioned earlier, nonlinear effects are mild over the entire region (the amplitude to depth ratio of the tides is $O(0.01)$). Thus, the residual circulation resulting from a combination of M_2 tidal forcing, river discharge and wind is *almost* a linear superposition of the current residuals resulting from the separate application of these forcings. The M_2 tidal ellipses in Fig. 9 also illustrate this lack of influence of river inflow and wind stress on tides.
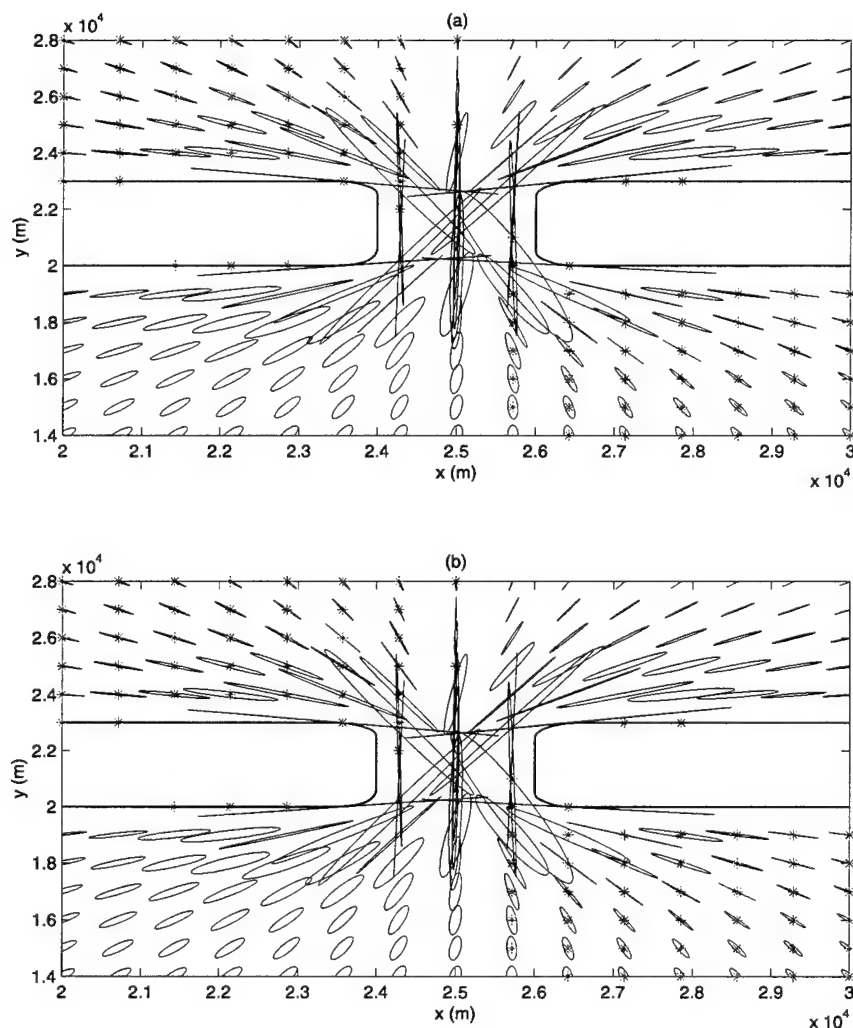

Fig. 9 – M_2 tidal ellipses: (a) Tidal forcing only; (b) With tidal forcing, river runoff, and wind forcing ("stars" indicate counter-clockwise rotating flow)

Figure 10 shows the evolution of the depth-averaged velocity fields every 1/6 of an M_2 tidal period (approximately every two hours). In Fig. 10(a) (flood tidal cycle), the flow is directed toward the bay. The flow converges uniformly into the inlet from the ocean side, is directed along the channel inside the inlet, and diverges away from the inlet in the bay. Figure 10(b) shows the velocity field just prior to the slack
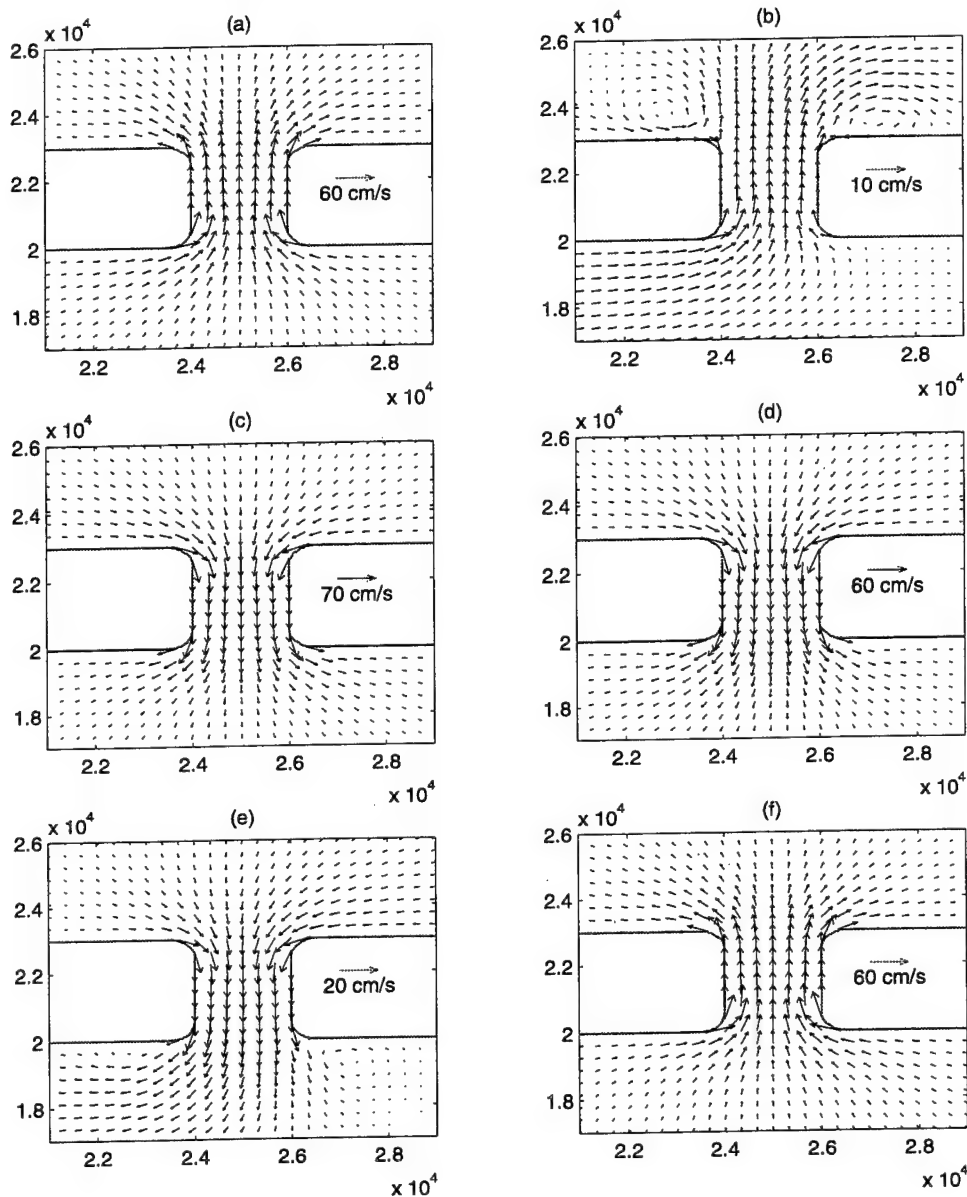
Fig. 10 – Tidal currents every 1/6th of a tidal period from (a) close to maximum
flood - through (f) a full tidal cycle

period between flood and ebb tide. At this time, gyres that form north of the inlet are clearly visible. It was noted earlier that the residual velocity fields as well as the amplitudes inside the bay are symmetric about the centerline of the inlet. Near the slack period, when the tidal velocities do not dominate and signatures of the residual circulation are expected to be more apparent, we anticipate similar symmetrical features in the currents and elevation. This however, is not the case here. The flow into the inlet is predominantly from the west and the eastern gyre in the bay is closer to the shoreline. Figures 10(c) and 10(d) show the velocity field during the ebb tide, before, and after maximum ebb is reached. Gyres inside the bay have disappeared and the flow is, as expected, almost exactly the reverse of that during the flood tide. Note that at these times the flow is almost symmetric about the centerline of the inlet. The influence of Coriolis acceleration terms starts to become apparent in Fig. 10(d). The beginnings of the gyre formation on the ocean side of the inlet are seen in Fig. 10(e), before the slack period between ebb and flood tide is reached. The Coriolis effect is now clearly visible. The tidal cycle is completed in Fig. 10(f), which again shows the flow field near the flood tidal phase, but before maximum flood tide is reached.

The Three-Dimensional Flow Field

We now investigate the three-dimensional residual flow field resulting from tidal forcing, wind forcing, and river discharge. The depth-averaged residual current (discussed in the previous section), the current at the surface, the current at mid-depth, and the near-bottom current forced by an M_2 tide at the offshore boundary are shown in Figs. 11(a)-(d) respectively. The surface currents (Fig. 11(b)) have magnitudes larger than the depth-averaged currents. Outside the inlet, the flow patterns are essentially the same as the depth-averaged patterns. Inside the inlet, the flow converges to approximately the center of the inlet from the sidewalls, whereas it diverges along the axis of the inlet, giving rise to a saddle-point (or stagnation point) close to the center. The mid-depth currents (Fig. 11(c)) also have the same features as the surface currents outside the inlet. Inside the inlet, the velocity directions are almost exactly opposite those seen in the surface currents. This results in additional stagnation points along the centerline close to either end of the inlet. The currents near the bottom show that eddies seen at the other levels are no longer present. Also, the currents outside the inlet are now directed toward the inlet. Inside the inlet, there is again one stagnation point in the center. Away from the centerline, the flow is directed toward the walls, similar to the mid-depth current pattern, although flow along the axis is stronger.
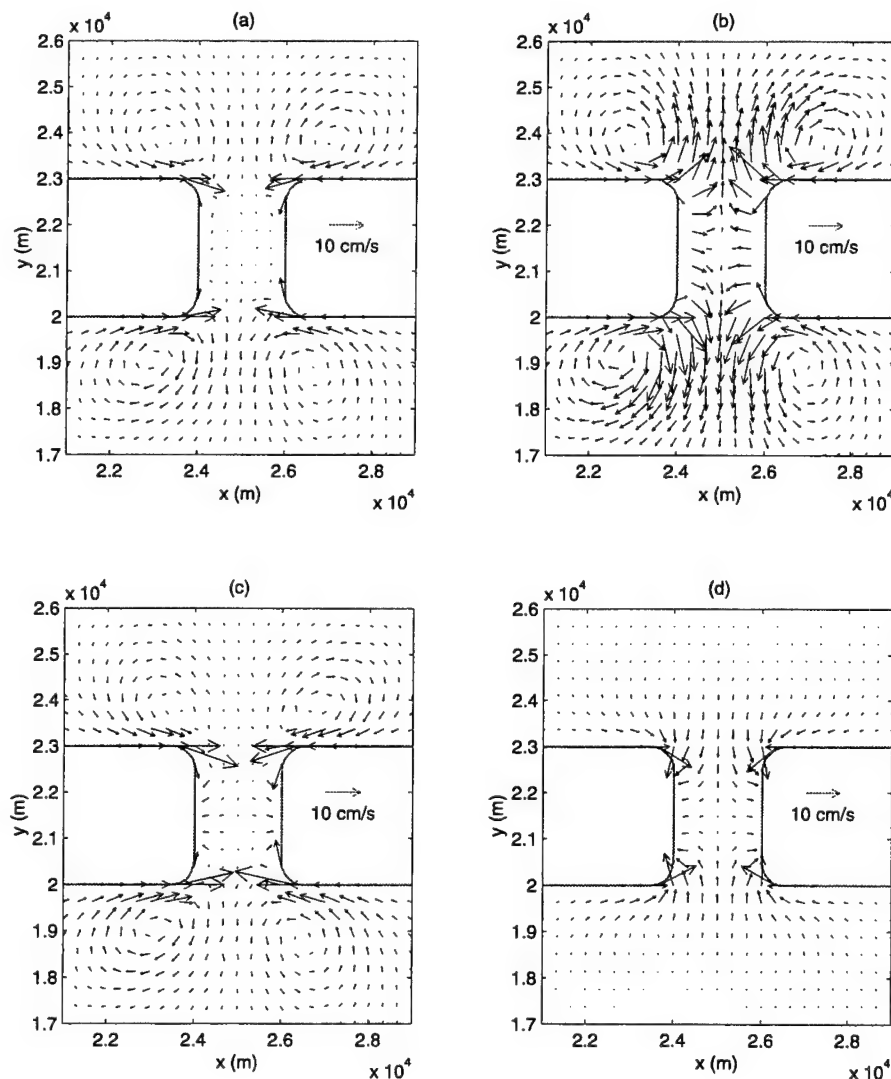

Fig. 11 – Residual currents forced by an M_2 tide: (a) Depth-averaged current; (b) Surface current; (c) Current at mid-depth; (d) Near-bottom current

To further illustrate some of the features described above, Fig. 12 shows the vertical velocity profiles at different locations in the inlet region. The top panel contains the velocity profiles at the northernmost position of the inlet near the embayment. The profiles in the middle panel are at the midpoint of the inlet, and the profiles in the lower panel are located at the southern entrance to the inlet. Also in Fig. 12, profiles in the leftmost column are positioned along the left side of the inlet; profiles in the center column correspond to the centerline of the inlet; those in the rightmost column are those along the right side of the inlet. The u-velocity in Fig. 12 is shown as a solid line and the v-velocity is a dashed line. We see that along the centerline of the inlet, the magnitude of the cross-channel flow is very small. The along-channel flow north and south of the inlet enters the inlet through the bottom part of the water column and exits the inlet along the surface.
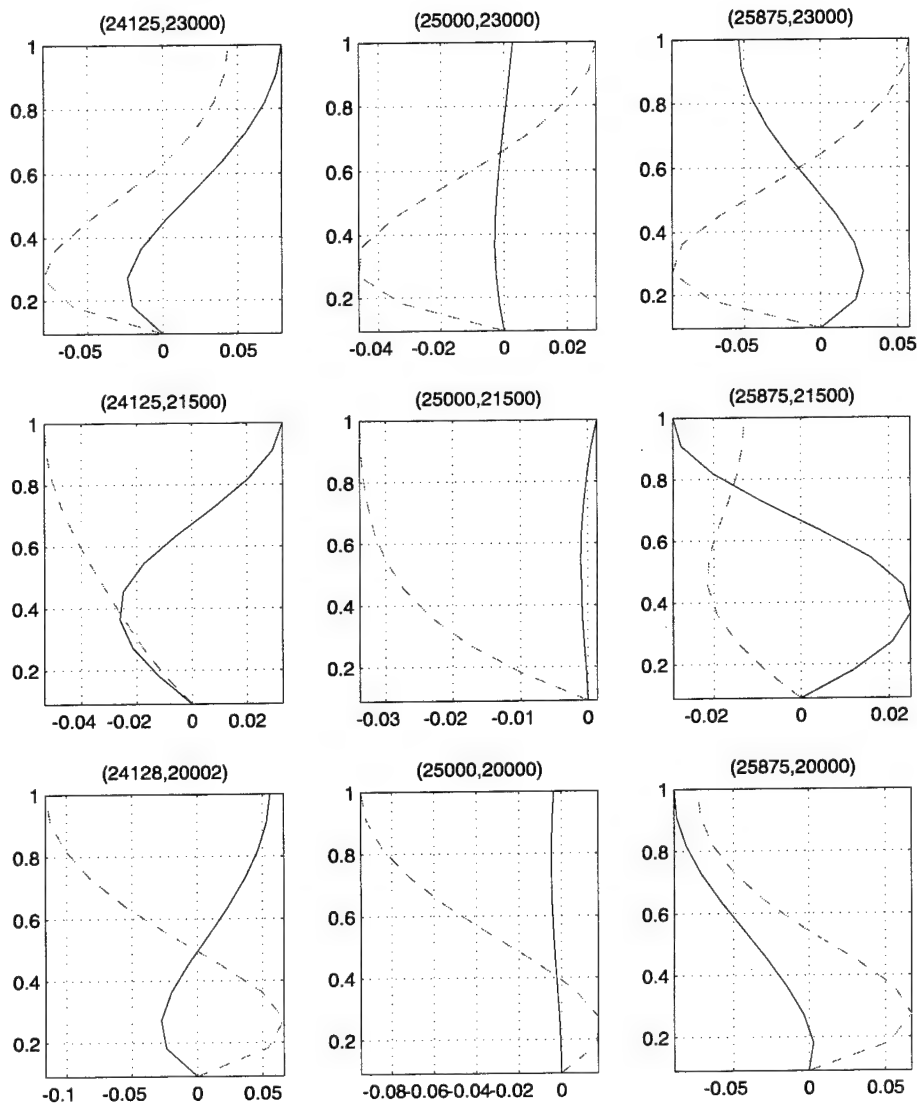

Fig. 12 – Velocity profiles at nine locations in the inlet. The (x, y) coordinates of the locations are shown on the figures. Solid line is the velocity in the x-direction; dashed line is the velocity in the y-direction; $y = 24000$ is the western shore, $y = 26000$ is the eastern shore, $x = 20000$ is the southernmost point, and $x = 23000$ is the northernmost point of the inlet.

Now we consider the three-dimensional residual currents forced by only wind (Fig. 13). The depth-averaged current (Fig. 13(a)), the surface current (13(b)), the current at mid-depth (13(c)), and the near bottom current (13(d)) all appear quite similar in pattern to each other in the region of the inlet and in the embayment. The primary difference is an increase in magnitude of the current from bottom to the surface. Near the inlet and in the embayment, the current direction is oriented at an angle of 45° to the right of the direction of the wind, which implies that the Ekman spiral is not present. Away from the inlet toward the open boundary, we see that the spiral is present to a certain degree, with currents oriented more toward the wind. This is even more pronounced in the near-bottom velocities. In an infinite ocean in the presence of wind, we expect to see the Ekman spiral, i.e., we expect the direction of the current to slowly change with increasing depth, until the near-bottom current is directed toward the shoreline. As mentioned before, this spiral is not reproduced here due to mass conservation. The boundaries on the east and west side are treated as solid wall, which means that there is no flow through those boundaries. However, with the depth-average current still pushing the water offshore to conserve the mass in the domain, a western boundary current is set up along the wall. Since there is free slip along the boundary walls, the western boundary current does not penetrate into the deeper coastal waters. Hence, over nearly the entire shelf region, the current is directed toward the open boundary.
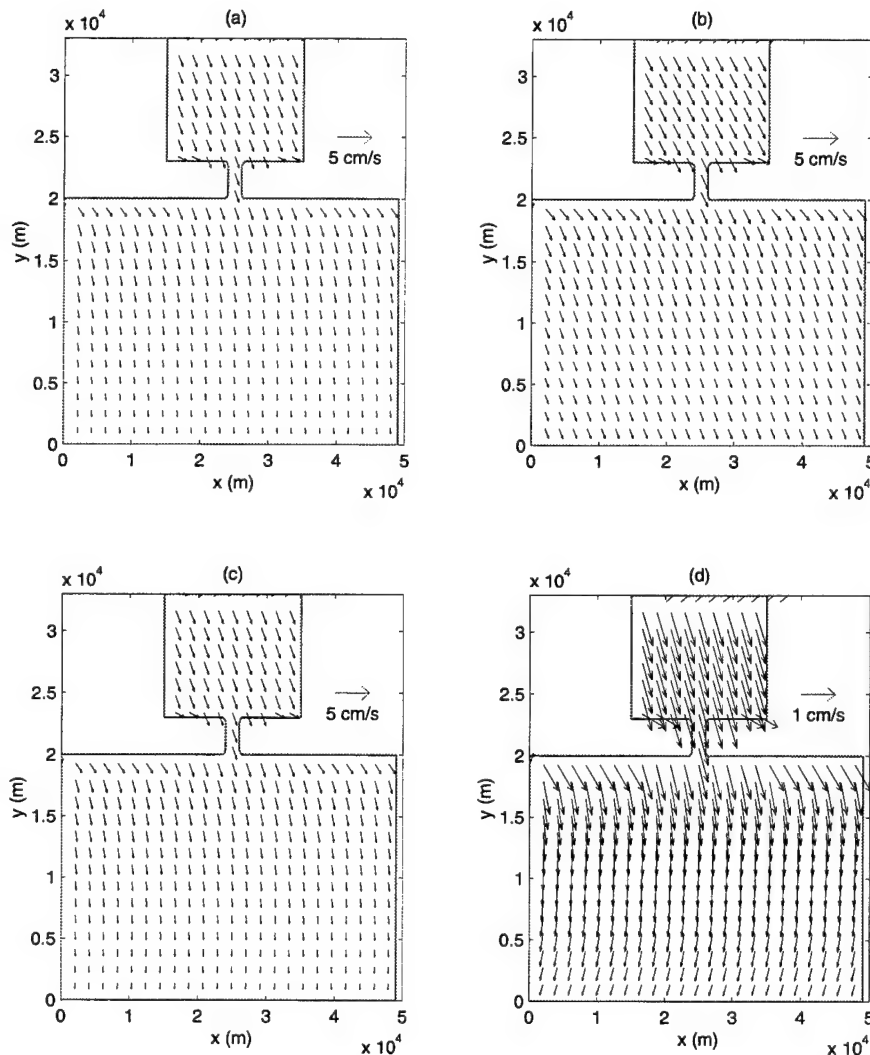

Fig. 13 – Wind-driven currents: (a) Depth-averaged current; (b) Surface current;
(c) Mid-depth current; (d) Near-bottom current

No such circulation is set up with the river outflow since the mass flowing out of the domain through the open boundary is replenished at the river boundary. Figure 14 shows that, as expected, the current set up by the river converges into the inlet and diverges into the coastal ocean. Comparing to the residual circulation induced by the tides in the absence of convection (Fig. 6), the flows are remarkably similar. From this, we infer that the effect of the convective acceleration term is negligible.
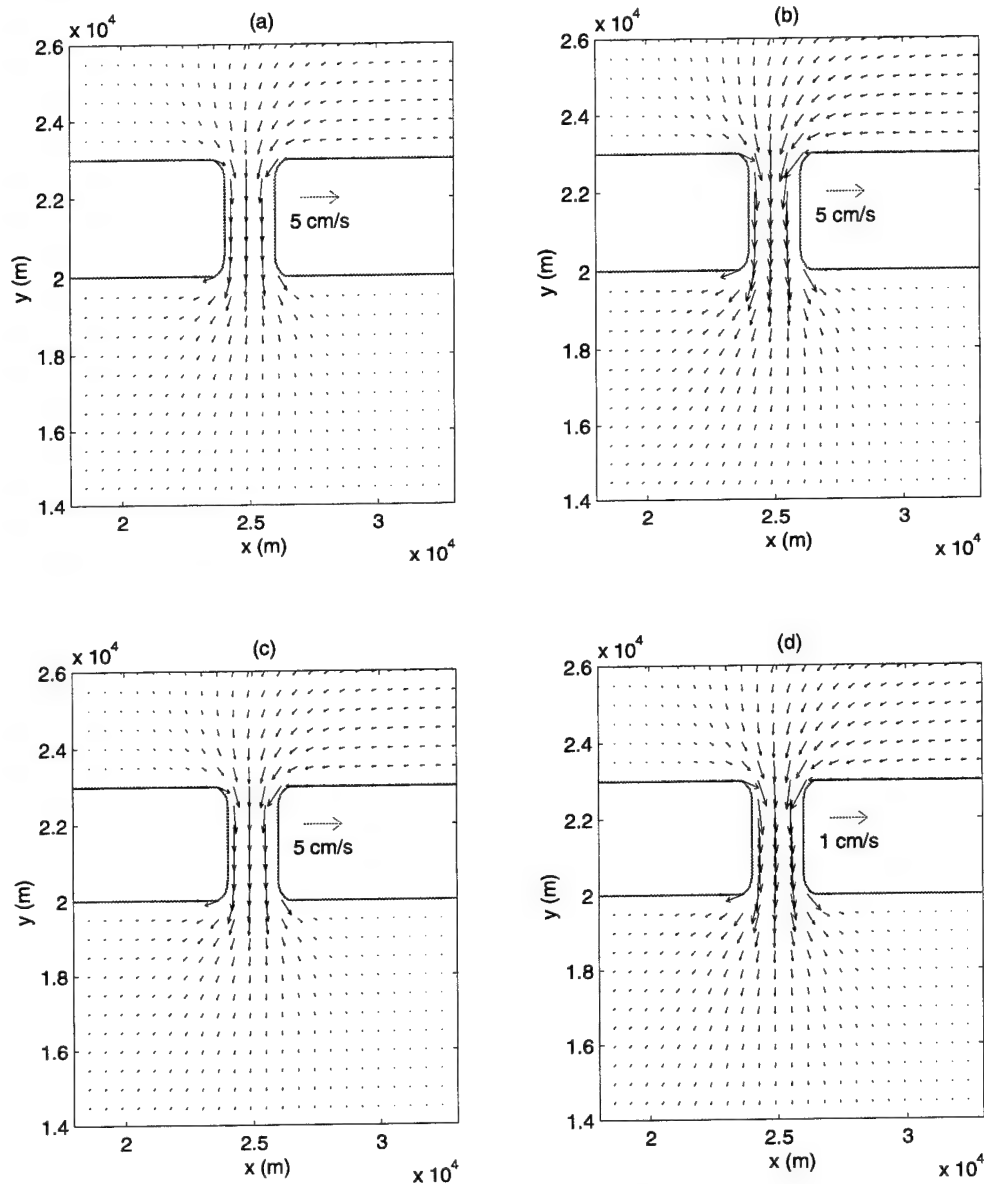

Fig. 14 – Current generated by river runoff: (a) Depth-averaged current; (b) Surface current;
(c) Mid-depth current; (d) Near-bottom current

Effect of a Barrier Island

We now investigate circulation in the vicinity of an inlet that is partially blocked on the ocean side by a barrier island as shown in Fig. 1(b). Figure 15 shows the residual current generated by normally incident M_2 tidal amplitude of 0.15 m. The circulation inside the bay is similar to that when there is no
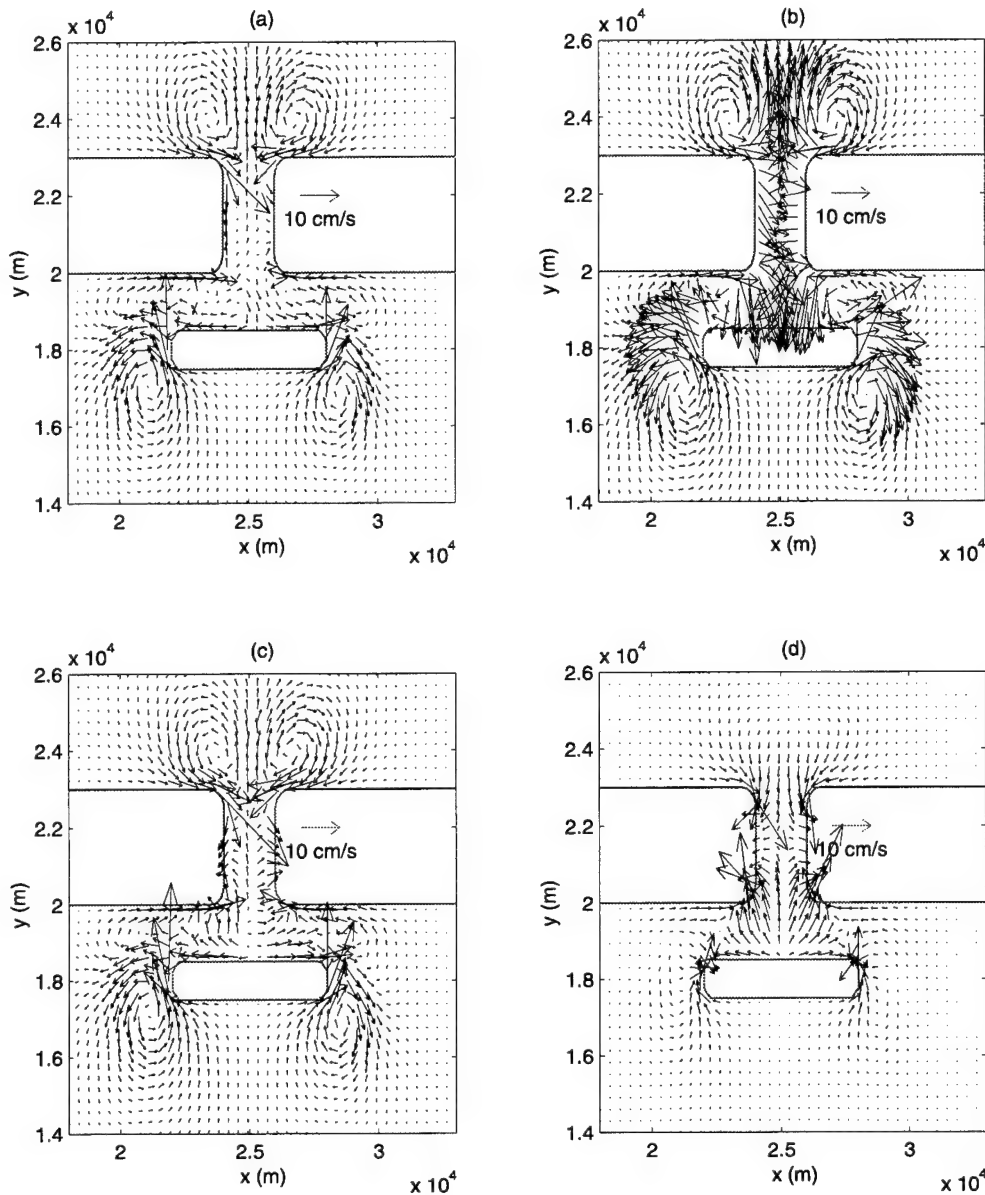
Fig. 15 – Residual currents forced by an M_2 tide in the vicinity of a partially blocked tidal inlet: (a) Depth-averaged current; (b) Surface current; (c) Current at mid-depth; (d) Near-bottom current

barrier island (Fig. 11), but within and seaward of the inlet the presence of the barrier island noticeably alters the flow patterns. The depth-averaged circulation (Fig. 15(a)) shows a stagnation point near the inlet entrance, with the direction of the flow in the inlet now toward the bay. This pattern sharply contrasts with that of Fig. 8(d) where the stagnation point is close to the center of the inlet. If the island were far enough from the mouth of the inlet, we would expect four eddies at the corners of the island in addition to the four eddies at the north and south end of the inlet. Here, the island is relatively close to inlet, so only two eddies form between the inlet and the island and two more eddies form south of the island. For the surface current (Fig. 15(b)) and the current at mid-depth (Fig. 15(c)), stagnation points are close to the mouth of the inlet near the bay. The stagnation point for the near-bottom current (Fig. 15(d)) is closer to the center of the inlet. Recall however for the case with no barrier island, the location of the stagnation points at all levels was near the center of the inlet. Notice also that while no eddies were present in the near-bottom current for the no barrier island configuration, eddies are evident here on the ocean side of the island.

The residual contours of the surface elevation (Fig. 16(a)) exhibit a depression of the water surface within the inlet. Contours of the M_2 tidal amplitude show, again, a gentler increase in amplitude along the eastern boundary of the inlet. The M_4 tidal amplitude forced by the M_2 tide (Fig. 16(c)), although larger than that obtained without the presence of the island, is still fairly small in comparison to the M_2 tidal amplitude. The tidal ellipses of the M_2 tide (Fig. 16(d)) show that the presence of the island causes the counter-clockwise rotation of the tides on the southwestern side of the island.
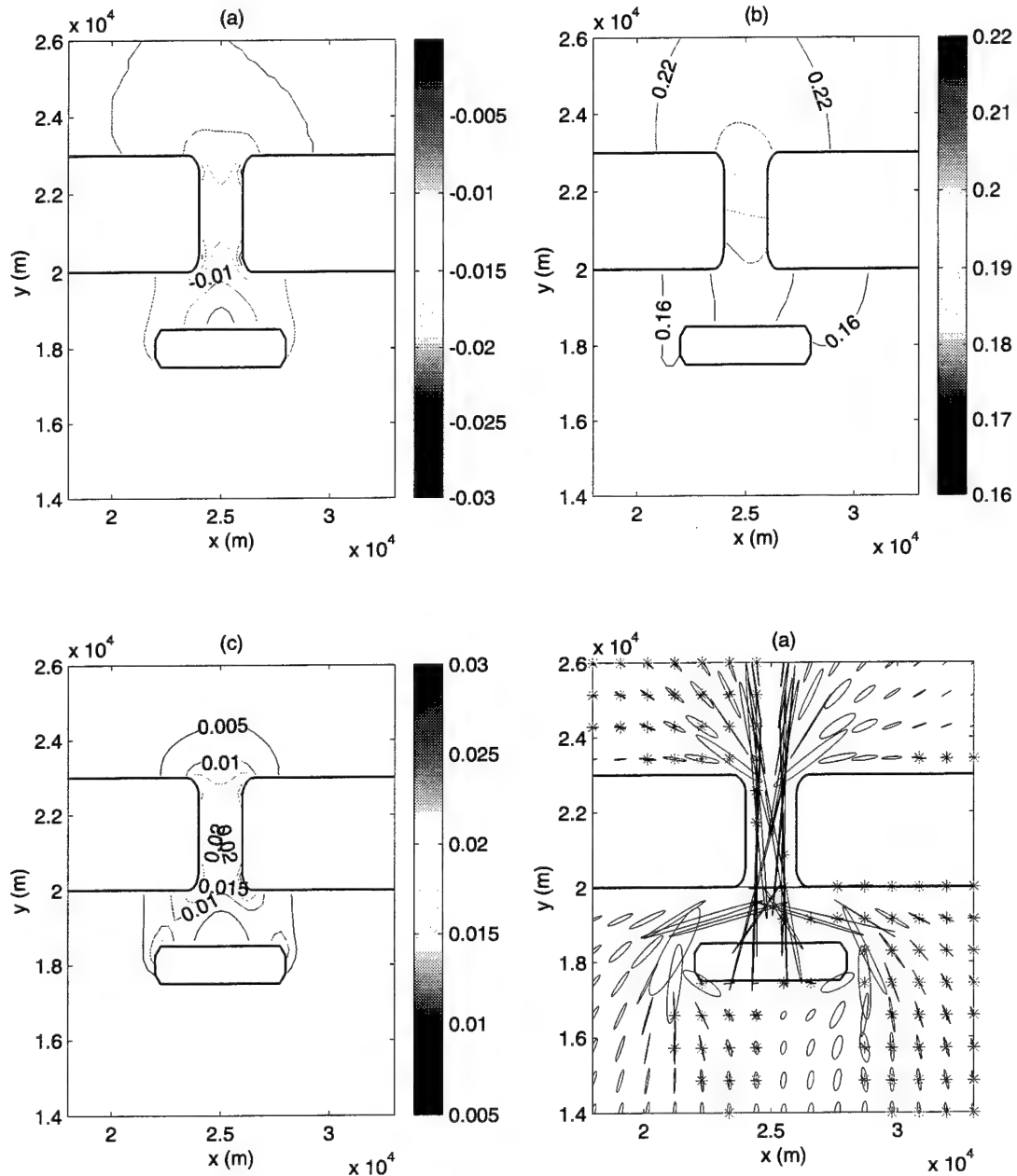

Fig. 16 – Amplitudes forced by an M_2 tide in the vicinity of a partially blocked tidal inlet ("stars" in the tidal ellipses indicate counter-clockwise rotating flow): (a) Residual amplitudes; (b) M_2 tidal amplitudes; (c) M_4 tidal amplitudes; (d) M_2 tidal ellipses

Figure 17 shows that the presence of the island does not influence the residual currents generated by the wind. The depth-averaged current, surface current, mid-depth current, and near-bottom current all look nearly identical to the case where there is no island (Fig. 13). Figure 18 shows that the presence of the island causes the residual flow induced by the river to separate, with the stagnation point at the center of the island. For these forcings, the flow is essentially linear, which implies that the convective acceleration terms do not play a role in the generated circulation dynamics.

CONCLUSIONS

ADCIRC, a finite-element model that has the option of being run in a two- or three-dimensional mode, is used to investigate the flow in the vicinity of an idealized tidal inlet. A series of numerical experiments are conducted to determine flow dynamics in and around an inlet and quantify model behavior when applied to such near-shore environments. The sensitivity of modeled dynamics to mesh resolution, dimensionality, and forcing frequency are considered. The effects of different forcing mechanisms such as tides, wind, and river runoff on the hydrodynamics near the inlet are studied individually and in combination. The tidal amplitude and phase are specified at the open boundary, wind is specified as a surface stress, and river runoff is specified as a flux boundary condition. In addition, the role of a barrier island offshore from an inlet is investigated.

Initially, a grid convergence study is conducted to determine the mesh resolution necessary to resolve the circulation dynamics in a bay, inlet, and shelf-system. A resolution of 100 m in and around the inlet is found to be sufficient for the applications here. All numerical experiments thereafter were performed using this grid. It is determined that the dynamics of the region are largely insensitive to whether a diurnal or semidiurnal forcing frequency is applied. Also, for the case of tidal forcing only, the 2D depth-averaged velocities and the surface elevations derived from the 3D model computations are similar to those computed with the 2D model. However, the computed solutions are significantly different for wind-driven river-forced dynamics. It was discovered that the Coriolis effect was negligible in the embayment, especially in comparison to the coastal ocean. The inclusion of convective acceleration terms is essential, even for weakly nonlinear flows such as the one studied here, to accurately represent the velocity field. The tidal amplitudes, on the other hand, are found to be not as sensitive to advection as the velocity field.

Counter-rotating eddies are set up in the residual velocity field at the entrances to the inlet by the tidal forcing. The flow field due to wind and river forcing alone shows no such feature. The depth-averaged flow in the inlet due to the combination of all of the above forcing is directed toward the ocean. In the absence of wind and river forcing, the velocities of currents in the inlet are very small. In contrast, three-dimensional flow patterns in the inlet are far more complicated. As expected, the surface currents are larger than the currents in the interior due to the effect of bottom friction. Vertical circulation cells are set up within the inlet such that in most areas, the direction of flow is reversed moving from surface to bottom. Kapolnai et al. (1996) saw similar features in their simulations, even when using a baroclinic model.

The presence of the barrier island does modify the tidally driven flow in the inlet. The depth-averaged flow is now directed away from the island through most of the water column in the inlet. However, the wind-driven currents and currents generated by the river are not significantly affected in the inlet by the presence of a barrier island.

As mentioned in the introduction, the principal aim of this study is to establish a database of results for an idealized tidal inlet that can be used to identify, analyze, and explain the processes in and near tidal inlets of the Mississippi Sound region in the northeast Gulf of Mexico. The idealized inlet domain without the barrier island is similar to the Bay of St. Louis, and the domain with the barrier island is similar to the
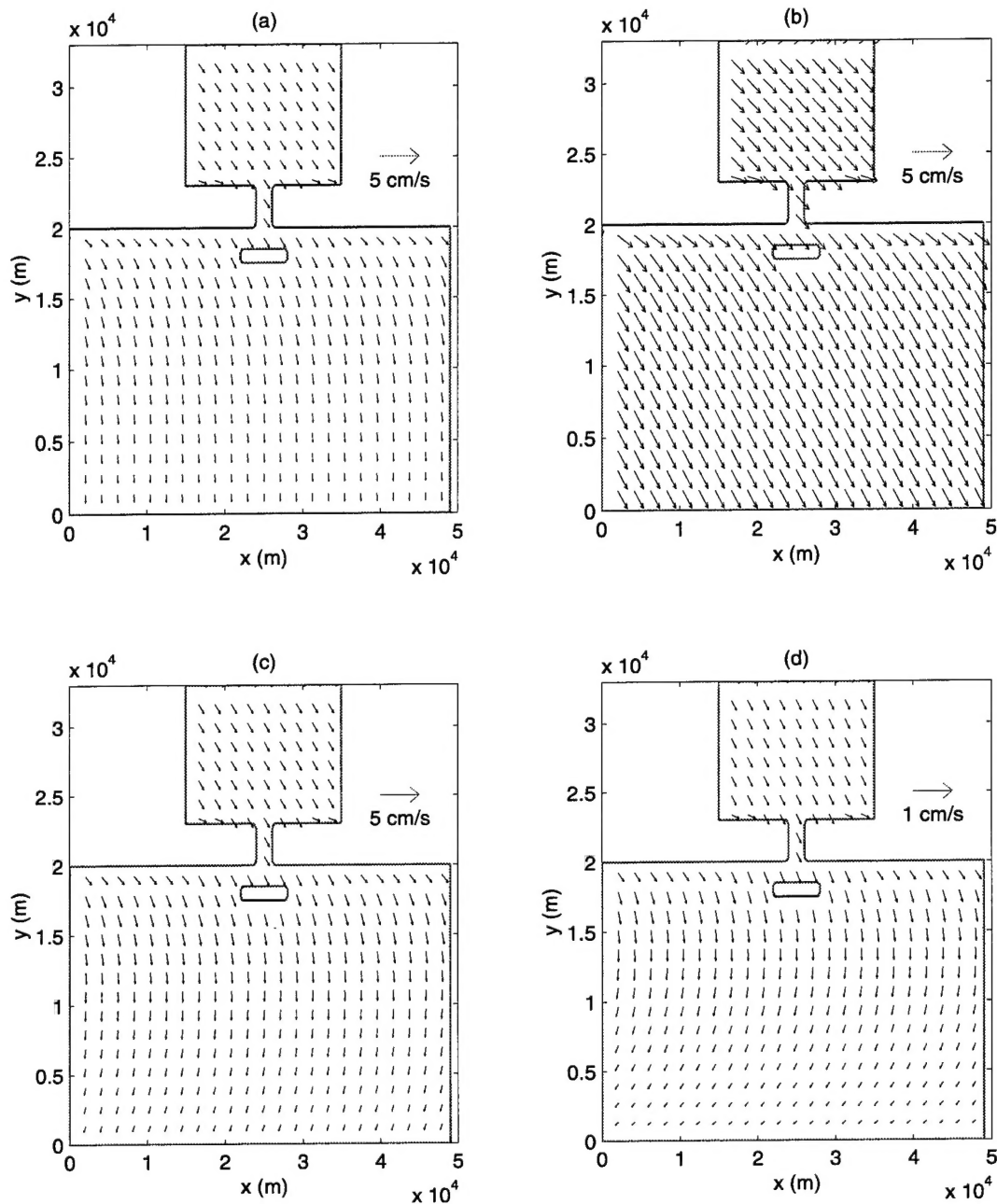
Fig. 17 – Wind-driven currents in the vicinity of a partially blocked tidal inlet: (a) Depth-averaged current; (b) Surface current; (c) Mid-depth current; (d) Near-bottom current

Back Bay of Biloxi. The water depths in realistic bays and the associated tidal inlets will be somewhat different than the constant value assumed here. Even so, the general circulation patterns as well as magnitudes of the velocities and amplitudes are expected to be similar to those described here.
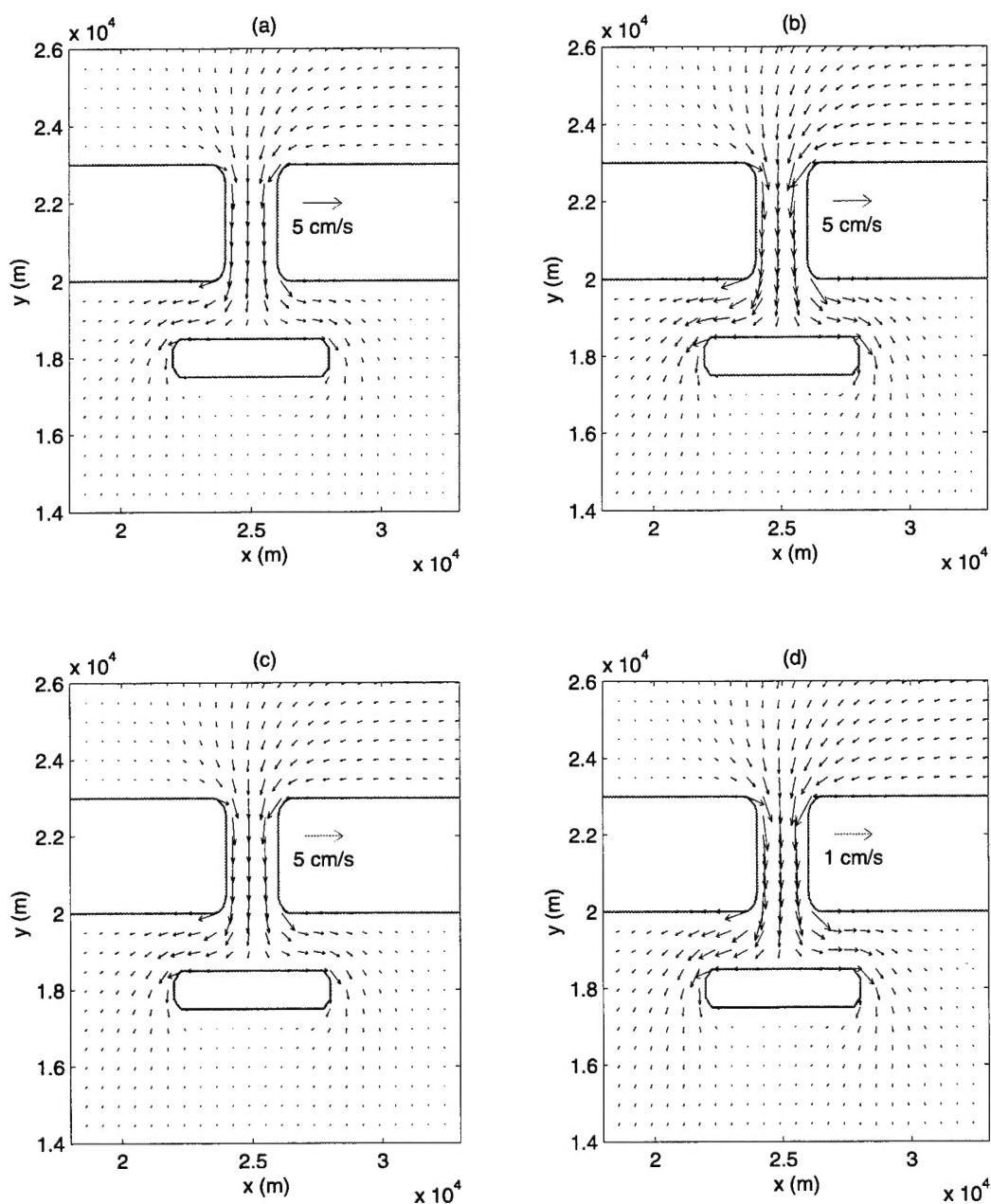
ACKNOWLEDGMENT

Fig 18 – Current generated by river runoff in the vicinity of a partially blocked tidal inlet: (a) Depth-averaged current; (b) Surface current; (c) Mid-depth current; (d) Near-bottom current

REFERENCES

Awaji, T., "Water Mixing in a Tidal Current and the Effect of Turbulence on Tidal Exchange through a Strait," *J. Phys. Oceanogr.* **12**, 501-514 (1982).

Awaji, T., N. Imasato, and H. Kunishi, "Tidal Exchange through a Strait: A Numerical Experiment Using a Simple Model Basin," *J. Phys. Oceanogr.* **10**, 1499-1508 (1980).

Blain, C.A. and W.E. Rogers, "Coastal Tide Prediction Using ADCIRC-2DDI Hydrodynamic Finite Element Model: Model Validation and Sensitivity Analyses in the Southern North Sea/English Channel," NRL/FR/7322-98-9682, December 1998.

David, L.T. and B. Kjerfve, "Tides and Currents in a Two-Inlet Coastal Lagoon: Laguna de Términos, México," *Cont. Shelf Res.* **18**, 1057-1079 (1998).

Imasato, N., S. Fujio, Q. Zhang, T. Awaji, and K. Akitomo, "Three-dimensional Numerical Experiments on Tidal Exchange through a Narrow Strait in a Homogeneous and Stratified Sea," *J. Oceanogr.* **50**, 119-139 (1994).

Kapolnai, A., F.E. Werner, and J.O. Blanton, "Circulation, Mixing, and Exchange Processes in the Vicinity of Tidal Inlets: A Numerical Study," *J. Geophys. Res.* **101**(C6), 14253-14268 (1996).

Kinnmark, I.P.E., "The Shallow Water Wave Equations: Formulation, Analysis and Application," Ph.D. dissertation, Department of Civil Engineering, Princeton University (1984).

Kolar, R.L. and W.G. Gray, "Shallow Water Modeling in Small Water Bodies," *Proc. 8ᵗʰ Int. Conf. Comp. Meth. Water Res.*, 39-44 (1990).

Kolar, R.L., W.G. Gray, J.J. Westerink, and R.A. Luettich, Jr., "Shallow Water Modeling in Spherical Coordinates: Equation Formulation, Numerical Implementation, and Application," *J. Hydr. Res.* **32**, 3-24 (1994a).

Kolar, R.L., J.J. Westerink, M.E. Cantekin and C.A. Blain, "Aspects of Nonlinear Simulations Using Shallow Water Models Based on the Wave Continuity Equation," *Comp. Fluids* **23**(3), 523-538 (1994b).

Grenier, R.R., Jr., R.A. Luettich Jr., and J.J. Westerink, "A Comparison of the Nonlinear Frictional Characteristics of Two-dimensional and Three-dimensional Models of a Shallow Tidal Embayment," *J. Geophys. Res.* **100**(C7), 13719-13735 (1995).

Luettich, R.A., Jr., J.J. Westerink, and N.W. Scheffner., "ADCIRC: An Advanced Three-dimensional Circulation Model for Shelves, Coasts and Estuaries, Report 1: Theory and Methodology of ADCIRC-2DDI and ADCIRC-3DL," Dredging Research Program Technical Report DRP-92-6, U.S. Army Engineers Waterways Experiment Station, Vicksburg, MS (1992).

Lynch, D.R. and W.G. Gray, "A Wave Equation Model for Finite Element Tidal Computations," *Comp. Fluids* **7**, 207-228 (1979).

Signell, R.P., and B. Butman, "Modeling Tidal Exchange and Dispersion in Boston Harbor," *J. Geophys. Res.* **97**, 15591-15606 (1992).

Westerink, J.J., R.A. Luettich, A.M. Baptista, N.W. Scheffner, and P. Farrar, "Tide and Storm Surge Predictions Using Finite Element Model," *ASCE J. Hydr. Eng.* **118**(10) 1373-1390 (1992a).

Westerink, J.J., R.A. Luettich, C.A. Blain, and N.W. Scheffner, "ADCIRC: An Advanced Three-dimensional Circulation Model for Shelves, Coasts and Estuaries, Report 2: Users's Manual for ADCIRC-2DDI," Dredging Research Program Technical Report DRP-92, U.S. Army Waterways Experiment Station, Vicksburg, Mississippi (1992b).

Westerink, J.J., R.A. Luettich, and J.C. Muccino, "Modeling Tides in the Western North Atlantic Using Unstructured Graded Grids," *Tellus* **46A**, 178-199 (1994).

Wheless, G.H. and A. Valle-Levinson, "A Modeling Study of Tidally Driven Estuarine Exchange through a Narrow Inlet onto a Sloping Shelf," *J. Geophys. Res.* **101**(C11), 25675-25687 (1996).